

MR-based camera-less eye tracking using deep neural networks

Markus Frey^{1,2,*}, Matthias Nau^{1,2,*†}, and Christian F. Doeller^{1,2,†}

¹Kavli Institute for Systems Neuroscience, NTNU, Trondheim, Norway

²Max-Planck-Institute for Human Cognitive and Brain Sciences, Leipzig, Germany

**joint first author, † joint senior author*

Abstract

Viewing behavior provides a window into many central aspects of human cognition and health, and it is an important variable of interest or confound in many fMRI studies. To make eye tracking freely and widely available for MRI research, we developed DeepMReye: a convolutional neural network that decodes gaze position from the MR-signal of the eyeballs. It performs camera-less eye tracking at sub-imaging temporal resolution in held-out participants with little training data and across a broad range of scanning protocols. Critically, it works even in existing datasets and when the eyes are closed. Decoded eye movements explain network-wide brain activity also in regions not associated with oculomotor function. This work emphasizes the importance of eye tracking for the interpretation of fMRI results and provides an open-source software solution that is widely applicable in research and clinical settings.

1 Introduction

2 Eye movements are a direct expression of our thoughts, goals and memories and where we look
3 determines fundamentally what we know about the visual world. The combination of eye track-
4 ing and neuroimaging can thus provide a window into many central aspects of human cognition,
5 along with insights into neurodegenerative diseases and neural disorders of the brain ([Anderson
6 & MacAskill, 2013](#)). A widely used tool to study human brain function is functional magnetic reso-
7 nance imaging (fMRI), which allows examining brain activity while participants engage in a broad
8 range of tasks. Viewing behavior is either a variable of interest or one of potential confound in
9 many fMRI studies, yet the very large majority of them does not perform eye tracking.

10 We argue that eye tracking can and should be a central component of fMRI research. Not only does
11 it allow in-depth insights into brain function, but it also offers a powerful behavioral read-out during
12 scanning. Importantly, eye movements are also associated with perceptual distortions ([Morrone et
13 al., 2005](#)), visual and motor activity ([Berman et al., 1999](#); [Petit & Haxby, 1999](#)) and imaging artifacts
14 ([McNabb et al., 2020](#)), which can severely affect the interpretation of neuroimaging results. If dif-
15 ferences in viewing behavior between experimental conditions remain undetected, there is a high
16 risk of misinterpreting differences in the observed brain activity. Crucially, this is not restricted to
17 studies of the visual system but affects task-based and resting-state neuroimaging on a large scale.

18 One example that illustrates the importance of eye tracking also for studies of higher-level cogni-
19 tion is the subsequent-memory effect, the observation that hippocampal activity during encoding
20 reflects whether a stimulus is later remembered or forgotten ([Wagner et al., 1998](#)). This effect is
21 often attributed to mnemonic processes in the hippocampus. However, because we also tend to
22 remember images better that we visually explored more thoroughly ([Kafkas & Montaldi, 2011](#)) and
23 because hippocampal activity scales with the number of fixations on an image ([Liu et al., 2017](#)), the
24 interpretation of hippocampal activity in this context can be difficult. In many such cases, it remains
25 unclear if the observed brain activity reflects higher-level cognitive operations or if it is driven by
26 viewing behavior ([Voss et al., 2017](#)).

27 MR-compatible camera eye trackers offer a solution. They track gaze position during scanning
28 and hence allow to analyze or account for gaze-related brain activity. In practice, however, camera-
29 systems are not applicable in many research and clinical settings, often because they are expensive,
30 require trained staff and valuable setup and calibration time, and because they impose experimen-
31 tal constraints (e.g. the eyes need to be open). Moreover, they cannot be used in visually impaired
32 patient groups or post-hoc once the fMRI data has been acquired.

33 An alternative framework is MR-based eye tracking: the reconstruction of gaze position directly
34 from the MR-signal of the eyeballs. While previous work suggested that this is indeed feasible
35 ([Tregellas et al., 2002](#); [Beauchamp, 2003](#); [Heberlein et al., 2006](#); [Son et al., 2020](#)), several critical
36 constraints remained that limited the usability to specific scenarios. These earlier approaches were
37 not as accurate as required for many studies, were limited to the temporal resolution of the imaging
38 protocol, and most importantly required dedicated calibration scans for every single participant.

39 Here, we present DeepMReye, a novel open source camera-less eye tracking framework based on a
40 convolutional neural network (CNN) that reconstructs viewing behavior directly from the MR-signal
41 of the eyeballs. It can be used to perform highly robust camera-less eye tracking in future fMRI-
42 experiments, but importantly also in datasets that have already been acquired. It decodes gaze po-
43 sition in held-out participants at sub-imaging temporal resolution, performs unsupervised outlier
44 detection and is robust across a wide range of viewing behaviors and fMRI protocols. Moreover,

45 it can create new experimental opportunities for example by performing eye tracking while the
46 eyes are closed (e.g. during resting-state or REM-sleep) or in patient groups for which eye-tracker
47 calibration remains challenging.

48 **Results**

49 In the following, we present our model and results in three sections. First, we introduce our
50 datasets, tasks, data processing pipeline and CNN in detail. Second, we show that the decoded
51 gaze positions are highly accurate and explore the applicability and requirements of DeepMReye
52 in depth. Lastly, by regressing the decoded gaze labels against the simultaneously recorded brain
53 activity, we show that viewing behavior explains activity in a large network of regions and that
54 DeepMReye can replace camera-based eye tracking for studying or accounting for these effects.
55 The approach and results presented below emphasize the importance of eye tracking for MRI re-
56 search and introduce a software solution that makes camera-less MR-based eye tracking widely
57 available for free.

58 **Decoding gaze position from the eyeballs using convolutional neural networks**

59 We demonstrate the wide applicability of our CNN-approach (Fig. 1AB) by decoding gaze from multi-
60 ple existing fMRI datasets with a total of 268 participants performing diverse viewing tasks (Fig. 1D)
61 including fixation (dataset 1, [Alexander et al., 2017](#)), smooth pursuit (dataset 2-4, [Nau et al., 2018a](#),
62 [2018b](#)), visual search (dataset 5, [Julian et al., 2018](#)) and free picture viewing (part of dataset 6). These
63 datasets were acquired on five 3T-MRI scanners using 14 scanning protocols. Repetition times (TR)
64 ranged between 800-2500ms and voxel sizes ranged between 1.5-2.5mm. The eyeballs of each
65 participant were first co-registered non-linearly to those of our group-average template, which
66 was obtained by averaging the functional images of all participants in dataset 4 ([Nau et al., 2018a](#))
67 fixating at the screen center. For each participant, we first aligned the head, then a facial bounding
68 box and finally the eyeballs to the ones of our template. This three-step procedure ensured that
69 the eyeballs were aligned across participants and that the average gaze position reflected center
70 fixation. The template brain has itself been co-registered to an MNI-structural template in which
71 the eyes were manually segmented (Fig. 1A). We then extracted the multi-voxel-pattern (MVP)
72 of the eyes at each imaging acquisition, normalized the pattern in time and space (Fig. 1B) and fed it
73 into the CNN (Fig. 1C). While the exact model training and test procedure will be explained in detail
74 later, it essentially uses the MVP of the eyes to predict 10 on-screen gaze coordinates correspond-
75 ing to the respective volume. For the main analyses, these 10 gaze labels per TR were obtained
76 either using camera-based eye tracking in case of the unconstrained visual search dataset ([Julian](#)
77 [et al., 2018](#)), or from the screen coordinates of the fixation target in case of all others ([Alexander](#)
78 [et al., 2017](#); [Nau et al., 2018a, 2018b](#)). For the final model evaluation, these 10 gaze labels were
79 median-averaged to obtain one gaze position per TR. The CNN was trained using cross-validation
80 and a combination of two weighted loss functions (Fig. 1C): 1) the 'Euclidean error' between real and
81 predicted gaze position and 2) a 'predicted error'. The latter represents an unsupervised measure
82 of the expected Euclidean error given the current input data.

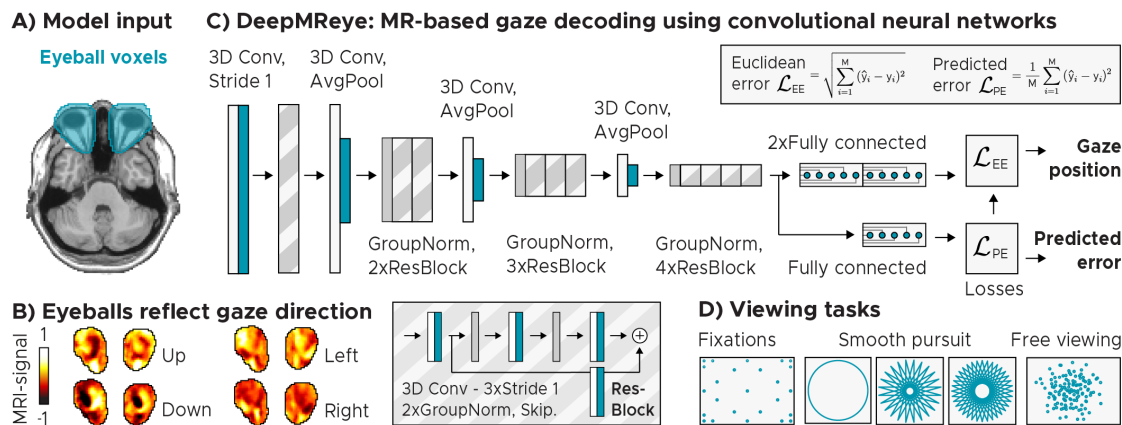


Figure 1: Model architecture and input. A) Manually delineated eye masks superimposed on T1-weighted structural template (Colin27) at MNI-coordinate Z = -36. B) Eyeball MR-signal reflects gaze direction. We plot the normalized MR-signal of eye-mask voxels of a sample participant who fixated a target on the left (X,Y = -10,0°), right (10,0°), top (0, 5.5°) or bottom (0, -5.5°) of the screen. C) Convolutional neural network architecture. The model takes the eye-mask voxels as 3D-input and predicts gaze position as a 2D (X, Y) regression target. It performs a series of 3D-convolutions (3D Conv) with group normalizations (GroupNorm) and spatial downsampling via average pooling (AvgPool) in between. Residual blocks (ResBlock) comprise an additional skip connection. The model is trained across participants using a combination of two loss functions: 1) The Euclidean error between the predicted and the true gaze position, and 2) the error between the Euclidean error and a predicted error. It outputs gaze position and the predicted error as a decoding-confidence measure for each TR. D) Schematics of viewing tasks. We trained and tested the model on data of 268 participants performing fixations (Alexander et al., 2017), smooth pursuit on circular or star-shaped trajectories (Nau et al., 2018a, 2018b) and free viewing (Julian et al., 2018).

83 Decoding viewing behavior in held-out participants

84 First, we examined the decoding performance in five key datasets that were acquired for other purposes (datasets 1-5, see Methods, Fig. 2, Alexander et al., 2017; Nau et al., 2018a, 2018b; Julian et al.,
85 2018). The model was trained and tested using an across-participant decoding scheme, meaning
86 that it was trained on 80% of the participants within each dataset and then tested on the held-out
87 20% of participants of that dataset. This procedure was cross-validated until all participants were
88 tested once. For all viewing behaviors we found that the decoded gaze path followed the ground
89 truth gaze path closely in the majority of participants (Fig. 2A). To quantify gaze decoding on the
90 group level, we computed three measures: the Euclidean error (EE, Fig. 2B, S1), the Pearson
91 correlation (r, Fig. 2C) as well as the coefficient-of-determination (R^2 , Fig. S2A) between the real
92 and the decoded gaze paths of each participant. We found that gaze decoding worked in the large
93 majority of participants with high precision (Fig. 2C, Fig. S2B) and for all viewing behaviors tested
94 (Median performance of the 80% most reliable participants (low predicted error): All datasets: [r
95 = 0.89, R^2 = 0.78, EE = 1.14°], Fixation: [r = 0.86, R^2 = 0.74, EE = 2.89°], Pursuit 1: [r = 0.94, R^2 =
96 0.89, EE = 0.64°], Pursuit 2: [r = 0.94, R^2 = 0.88, EE = 1.14°], Pursuit 3: [r = 0.86, R^2 = 0.72, EE =
97 1.11°], Free viewing: [r = 0.89, R^2 = 0.78, EE = 2.17°]). These results were robust also when independent
98 data partitions of each participant were used for training and test (within-participant decoding
99 scheme, Fig. S4A), and that DeepMRReye uncovered gaze position even when independent datasets
100 were used for model training and test (across-dataset decoding, Fig. S4B). Together, these results
101 demonstrate that gaze decoding with DeepMRReye can be highly reliable and accurate. It allows
102 reconstructing even complex viewing behaviors in held-out participants and detects outliers in an
103 unsupervised fashion. Critically, it does so by relying solely on the MR-signal of the eyeballs without
104 requiring any MR-compatible camera equipment.
105

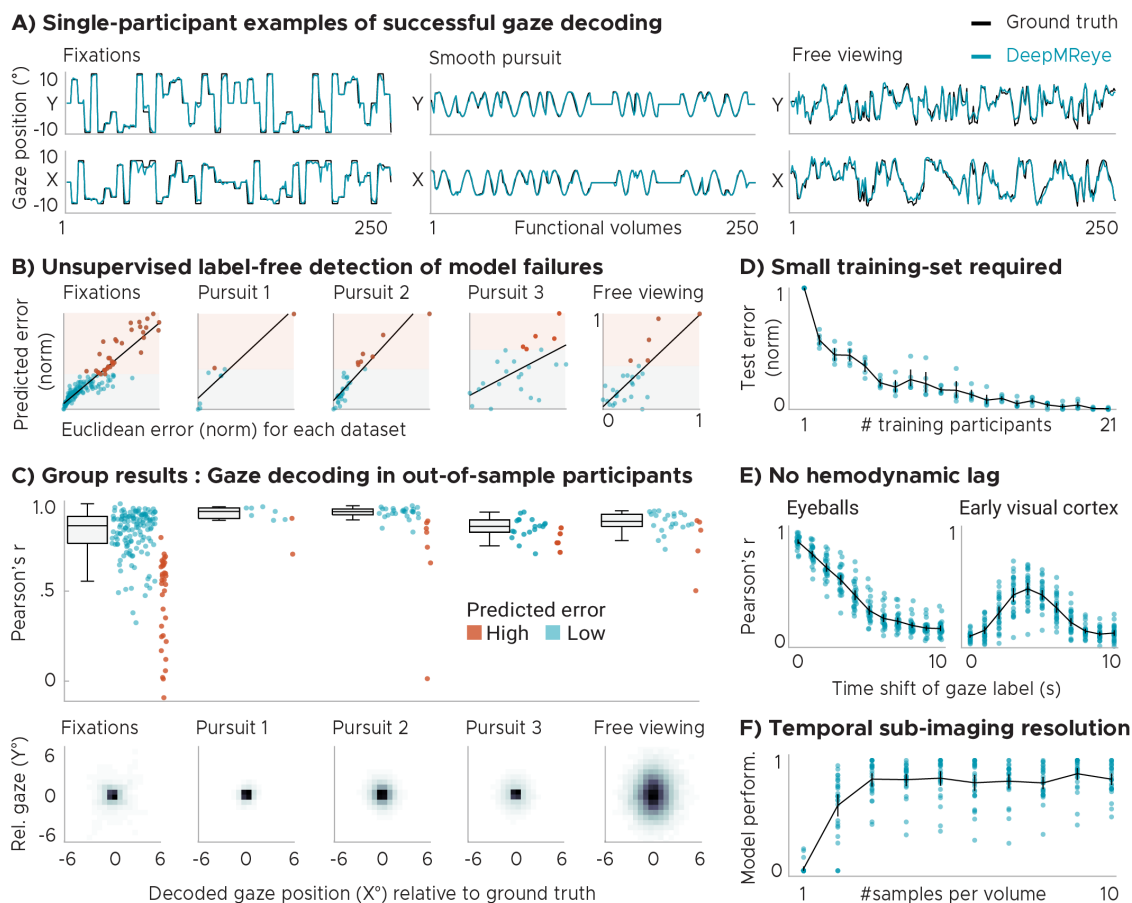


Figure 2: Across-participant gaze decoding results. A) Single-participant examples of successful gaze decoding for three viewing behaviors. B) Predicted error (PE) correlates with the Euclidean error between real and predicted gaze positions. This allows filtering the test set post-decoding based on estimated reliability. We plot single-participant data with regression line. Participants were split into 80% most reliable (Low PE, blue) and 20% least reliable participants (high PE, orange). Scores normalized for visualization. C) Group results: Top panel shows gaze decoding expressed as the Pearson correlation between true and decoded gaze trajectory for the five key datasets featuring fixations, 3x smooth pursuit and visual search. Participants are color coded according to PE. We plot Whisker-box-plots for Low-PE participants and single-participant data for all. Bottom panel shows time-collapsed group-average histograms of decoded positions relative to the true positions [0,0] in visual degrees. Color depicts decoding probability (black = high). D) Test error as a function of how many participants were used for model training. E) Gaze decoding from the eyeballs and early visual cortex for time-shifted gaze labels. F) Sub-imaging temporal resolution: We plot the model performance (explained variance normalized for each participant) depending on how many sub-imaging samples were decoded. D-F show results for visual search dataset 5.

106 Unsupervised outlier detection

107 As mentioned above, the model computes a predicted error score for each sample and participant
 108 in addition to decoding gaze position. Importantly, this predicted error correlated with the true
 109 Euclidean error across participants, allowing to detect participants for which the decoding did not
 110 work well (Fig. 2B, Fig. S1AB). It can thus be used to remove outliers from subsequent analysis
 111 or to account for them for example by adding covariate regressors in group analyses. Note that
 112 besides detecting outlier participants, the predicted error also allowed removing outlier-samples
 113 within each participant, which further improved the reliability of the results (Fig. S3).

114 **No camera required for model training**

115 We next explored our model's requirements and boundary conditions in detail. First, we tested
116 what type of training labels are required for DeepMReye, finding that both the screen coordinates
117 of a fixation target (Fig. 2C) and labels obtained using camera-based eye tracking (Fig. S5) led
118 to similar performance. While the results presented for dataset 5 (Fig. 2C) already reflect the
119 ones obtained with camera-based labels, we additionally re-ran the model on gaze labels obtained
120 via camera-based eye tracking also for the smooth pursuit datasets 3-4 (Fig. S5). Thus, because
121 DeepMReye can be trained on fixation-target labels only, and because it generalizes across par-
122 ticipants (Fig. 2), users could acquire fMRI data for a few participants performing various fixation
123 tasks, record the screen coordinates of the fixation target as training labels, train the model on
124 these labels and then decode from all other participants. Upon publication, we will provide the
125 code for an experimental paradigm that can be used to produce such training labels (see 'Data and
126 code availability' statement and 'User recommendation' section).

127 **Small training set**

128 Next, we asked how many participants were required for model training. We tested this by itera-
129 tively sub-sampling the number of participants in the training set, each time testing how well the
130 model performed on the same test participants. We chose to conduct this analysis on the data of
131 dataset 5 because it featured the most natural and hence most complex viewing pattern tested. We
132 found that model performance improved with an increasing training set size, but also that model
133 performance already reached a ceiling level at as few as 6-8 participants (Mean performance, 1
134 participant: [$r = 0.43$, $R^2 = 0.11$, $EE = 5.12^\circ$], 5 participants: [$r = 0.81$, $R^2 = 0.62$, $EE = 3.18^\circ$], 10 partic-
135 ipants: [$r = 0.86$, $R^2 = 0.71$, $EE = 2.58^\circ$], Fig. 2D, Fig. S6). This suggests that even a small training set
136 can yield a well-trained model and hence reliable decoding results. Model performance likely also
137 depends on how much data is available for each participant and on how similar the expected view-
138 ing behavior is between training and test set. If the gaze pattern is very similar across participants,
139 which can be the case even for viewing of complex stimuli such as real-world scenes (Ehinger et al.,
140 2009), decoding it in independent participants can work even better despite a small training set.
141 This fact can be seen for example in our main results for the smooth-pursuit dataset 2 (Nau et al.,
142 2018b, Fig. 2).

143 **No hemodynamic component**

144 Naturally, when the eyes move, the surrounding tissue undergoes dramatic structural changes,
145 which are expected to affect the MR-signal acquired at that time. To test whether this is the source
146 of information used for decoding, we shifted the gaze labels relative to the imaging data by vari-
147 ous TR's (0-10), each time training and testing the model anew. Indeed, we found that the eyeball
148 decoding was most accurate for the instantaneous gaze position and that no hemodynamic fac-
149 tors needed to be considered (Fig. 2E). This is in stark contrast to decoding from brain activity for
150 which the same model pipeline can be used (Fig. 2E). In V1, decoding was optimal after around 5-6
151 seconds ($r=0.483 \pm 0.132$) and followed the shape of the hemodynamic response function (HRF).

152 **Sub-imaging temporal resolution**

153 Intriguingly, because different imaging slices were acquired at different times and because the MR-
154 signal of a voxel can be affected by motion, it should in principle be possible to decode gaze posi-
155 tion at a temporal resolution higher than the one of the imaging protocol (sub-TR resolution). As

156 mentioned above, DeepMReye classifies 10 gaze labels per functional volume, which are median-
157 averaged to obtain one gaze position per TR. This procedure yielded a higher decoding perfor-
158 mance compared to classifying only one position, and it enabled testing how well the gaze path
159 can be explained by the sub-TR labels themselves (Fig. S8A). We found that during visual search
160 more gaze-path variance was explained by decoding up to three positions per TR compared to
161 decoding only one position per TR (3Hz, Fig. 2F), which dovetails with the average visual-search
162 eye-movement frequency of 3Hz (Wolfe, 2020). Moreover, the 10 real and decoded sub-TR labels
163 varied similarly within each TR (Fig. S8B), which again suggests that within-TR movements could
164 be detected. While the exact resolution likely depends on the viewing behavior and the imaging
165 protocol, these results show that at least a moderate sub-imaging temporal decoding resolution is
166 indeed feasible.

167 **Across-dataset generalization**

168 The results presented so far show that the gaze decoding with DeepMReye is highly accurate
169 when the viewing behavior and the imaging protocol are similar between training and test set.
170 To test if our model also generalizes across datasets, we next implemented a leave-one-dataset-
171 out cross-validation scheme. Most datasets were acquired by different groups using different
172 MR-scanners, participants and viewing behaviors but with similar voxel sizes and TR's. While this
173 across-dataset scheme led to overall lower performance scores compared to the across-participant
174 (within-dataset) scheme presented earlier, it nevertheless recovered viewing behavior with remark-
175 able accuracy in all cases (Median performance of the 80% most reliable participants (low predicted
176 error): All datasets: [$r = 0.84$, $R^2 = 0.59$, $EE = 2.78^\circ$], Fixation: [$r = 0.79$, $R^2 = 0.52$, $EE = 5.34^\circ$], Pursuit
177 1: [$r = 0.88$, $R^2 = 0.64$, $EE = 1.47^\circ$], Pursuit 2: [$r = 0.86$, $R^2 = 0.65$, $EE = 2.15^\circ$], Pursuit 3: [$r = 0.85$, $R^2 =$
178 0.55 , $EE = 2.01^\circ$], Free viewing: [$r = 0.84$, $R^2 = 0.61$, $EE = 2.96^\circ$], Fig. S4). This suggests that datasets
179 acquired with similar fMRI protocols can be used for model training, even if the recording site or the
180 protocol were not exactly the same. Future investigations will need to quantify how larger differ-
181 ences in scan parameters affect this across-dataset generalization (e.g. different phase encoding
182 directions or slice tilts). Note that despite higher Euclidean error and lower R^2 -scores compared to
183 within-dataset decoding, the across-dataset decoding scheme led to relatively high Pearson corre-
184 lations. This indicates that the main reason for the lower performance scores is the scaling of the
185 decoding output relative to the test labels, likely because the data range of the training and testing
186 labels differed. Importantly, this also suggests that the presence of putative eye movements, but
187 not their correct amplitude, could still be detected accurately, which is the most important aspect
188 for many fMRI analyses or nuisance models.

189 **Robust across voxel sizes and repetition times**

190 Functional MRI protocols can differ in many aspects. Most importantly in this context, they can
191 differ in the spatial and temporal resolution of the acquired data (i.e. voxel size and TR). To explore
192 the influence of these two parameters on the decoding performance in detail, we varied them
193 systematically across 9 fMRI protocols for the acquisition of a sixth dataset. For each of the 9
194 sequences, we scanned 4 participants with concurrent camera-based eye tracking while they freely
195 explored pictures (Hebart et al., 2019) or performed fixation (Alexander et al., 2017) and smooth
196 pursuit tasks similar to the ones used earlier (Nau et al., 2018a, 2018b). DeepMReye decoded gaze
197 position robustly in this dataset 6 during all of these tasks and in all imaging protocols tested (3x3
198 design: TR = 1.25s, 1.8s, 2.5s, voxel size = 1.5mm, 2mm, 2.5mm, Fig. 3A), demonstrating that it is
199 widely applicable across a broad range of routinely used voxel sizes and TR's.

200 Eyes-closed tracking

201 Traditional MR-compatible eye-tracking systems typically detect certain features of the eyes such
202 as the pupil and/or the corneal reflection in a video, which are then tracked over time (Duchowski,
203 2017). When the relevant features are occluded or cut off on the video (e.g. when the eyes close),
204 the tracking is lost. Because our approach relies on the fact that the eyeball MR-signal changes as
205 a function of gaze position (Fig. 1B), it might be possible to decode gaze position, or in this case
206 more generally the state of the eyeballs, even when the eyes are closed. As a proof-of-concept, we
207 therefore tested in one participant of dataset 6 whether DeepMReye can uncover viewing behavior
208 even when the eyes are closed. The participant was instructed to close the eyes and move them
209 either repeatedly from left to right or from top to bottom, and to indicate the behavior via key press.
210 We trained DeepMReye on the diverse eyes-open viewing data from all participants in dataset 6 and
211 then decoded from the one participant while the eyes were closed. We found that the gaze pattern
212 decoded with DeepMReye closely matched the participant's self-report, suggesting that it is indeed
213 possible to perform eye tracking while the eyes are closed (see the 'User recommendation' section).
214

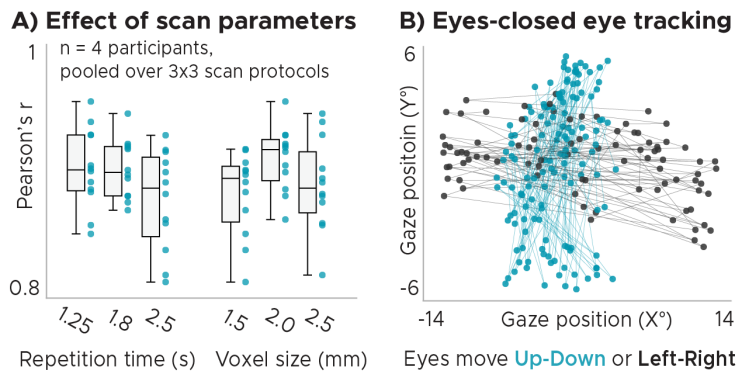


Figure 3: Effect of scan parameters and eye tracking while the eyes are closed. A) Effect of voxel size and repetition time (TR). We plot gaze decoding expressed as the Pearson correlation between true and decoded gaze trajectory for different voxel sizes and TR's. We plot Whisker-box-plots and single-participant data (n = 4) for 9 fMRI protocols collapsed either over TR or voxel size. DeepMReye recovered viewing behavior successfully in all sequences tested. B) Decoded gaze coordinates for a participant being instructed to move the eyes left & right or up & down while keeping them closed. Dots are colored based on button press of participant indicating movement direction.

215 Viewing behavior explains network-wide brain activity

216 The results presented so far demonstrate that DeepMReye can be used to perform eye tracking
217 in many experimental settings. A critical open question that remained was whether its decoding
218 output can be used to analyze brain activity. To test this, we implemented a whole-brain mass-
219 univariate general model (GLM) for the visual search dataset 5. We again chose this dataset be-
220 cause it featured the most complex viewing pattern tested. To simulate differences in viewing
221 behavior between the two conditions, we first computed an eye-movement index, reflecting the
222 Euclidean distance between gaze positions of subsequent volumes. We used this eye-movement in-
223 dex to build two main regressors of interest, one modeling large eye movements and one modeling
224 short eye movements. Both regressors were binarized and convolved with the hemodynamic re-
225 sponse function. Contrasting the model weights estimated for these two regressors was expected
226 to reveal regions in the brain whose activity is driven by viewing behavior such as the visual and
227 oculomotor (attention) network (Berman et al., 1999; Petit & Haxby, 1999).

228 To know what we were looking for, we first conducted this analysis using the gaze labels obtained
229 with traditional camera-based eye tracking and then compared the results to the ones obtained for
230 the three cross-validation schemes of DeepMReye (within-participants, across-participants, across-
231 datasets).

Decoded viewing behavior explains network-wide brain activity

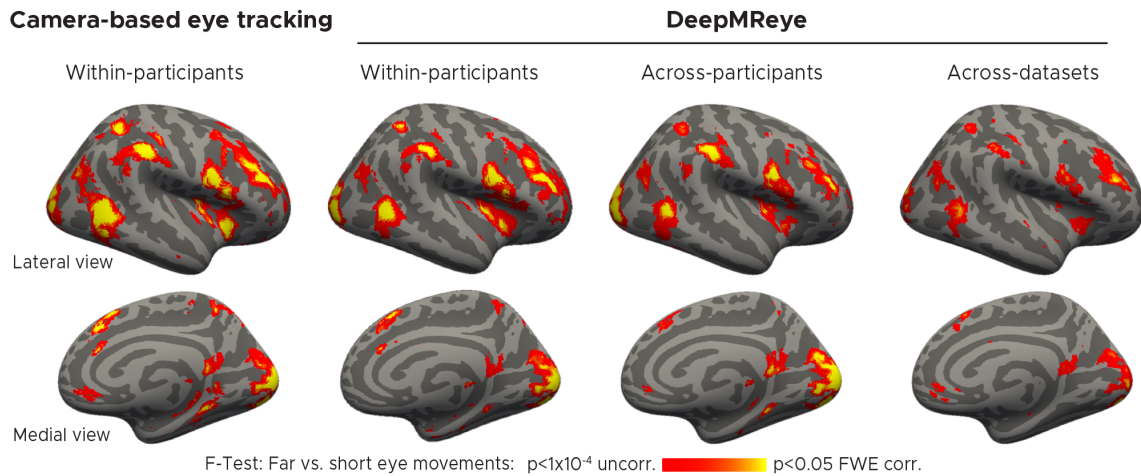


Figure 4: Decoded viewing behavior explains network-wide brain activity. General-linear-model (GLM) group results for the contrast 'Far vs. short eye movements' during visual search. We plot the F-statistic of this contrast superimposed on a template surface (fsaverage) for gaze-labels obtained with camera-based eye tracking (first panel) as well as for three DeepMReye cross-validation schemes. **Within-participants:** All participants of a dataset were included with different partitions in model training and test. **Across-participants:** Different participants were included during model training and test. **Across-datasets:** Different datasets (and hence also different participants) were included during model training and test.

232 As predicted, we found that viewing behavior explained brain activity in a large network of regions
233 (Fig. 4) including the early visual cortex, frontoparietal regions (likely the frontal eye fields), the pos-
234 terior parietal cortex as well as temporal lobe regions (likely including the human motion complex).
235 Importantly however, differences in viewing behavior also explained brain activity in regions not
236 typically associated with oculomotor function such as the ventromedial prefrontal cortex (vmPFC),
237 the anterior and posterior cingulate cortex, the medial parietal lobe (likely comprising the retros-
238 plenial cortex), the parahippocampal gyrus as well as the hippocampus (Fig. 4).

239 Strikingly, comparing the results obtained with DeepMReye to the ones obtained with camera-
240 based eye tracking showed an exceptional match between the two (Fig. 4). This was true for all
241 decoding schemes, including the across-participant decoding scheme, which can be conducted
242 even in existing datasets with some preparation (Fig. 2, see 'User recommendations'). Moreover,
243 even the across-dataset scheme explained gaze related variance on group level, despite the differ-
244 ences in the underlying viewing behaviors and imaging protocols.

245 Finally, because eye movements are associated not only with brain activity but also with imaging
246 artifacts, the MRI signal might also be affected instantaneously when the movement occurs. To
247 quantify these instantaneous effects, we repeated the GLM analysis modeling eye-movement re-
248 lated fluctuations in the MRI signal without accounting for the hemodynamic response. This vari-
249 ance is not captured by traditional head-motion regressors (Fig. S9). Again, we found that eye
250 movements explained signal variations in many brain regions (Fig. S10), likely reflecting a combi-
251 nation of imaging artifacts and instantaneous hemodynamic components (e.g. the initial dip).

252 Discussion

253 DeepMReye is a camera-less eye tracking framework based on a CNN that decodes gaze position
254 from the MR-signal of the eyeballs. It allows monitoring viewing behavior accurately and contin-
255 uously at a moderate sub-imaging resolution without the need for MR-compatible cameras. We
256 demonstrated that our approach works robustly for a wide range of voxel sizes and repetition
257 times as well as for various viewing behaviors including fixation, smooth pursuit, free viewing and
258 as a proof-of-concept even when the eyes were closed. For each gaze position and participant, the
259 model outputs an unsupervised predicted error score that can be used to filter out outliers even
260 when test labels are missing. A small training set can yield a well-trained model and high decoding
261 performance even when trained without camera-based labels. The decoded gaze positions and
262 eye movements can be used in subsequent fMRI analyses similar to camera-based eye tracking,
263 and doing so here revealed gaze-related activity in a large network of regions in the brain (Berman
264 et al., 1999; Petit & Haxby, 1999; Voss et al., 2017). Critically, by testing our model in independent
265 participants within each dataset, but also in participants in other datasets acquired with different
266 MR-scanners and protocols, we demonstrated the potential of DeepMReye to successfully decode
267 viewing behavior also in existing fMRI data.

268 MR-based gaze prediction

269 The present work is directly inspired by earlier reports showing that the MR-signal of the eyeballs
270 can be used to infer the state of the eyes during MRI-scanning. This includes movements of the
271 eyes (Tregellas et al., 2002; Beauchamp, 2003; Keck et al., 2009; Franceschiello et al., 2020), the
272 position of gaze on the screen (Heberlein et al., 2006; LaConte & Glielmi, 2006; Son et al., 2020;
273 Sathian et al., 2011; Keck et al., 2009) or whether the eyes were open or closed (Brodoehl et al.,
274 2016). Moreover, gaze position can be decoded from early visual cortex activity during scene view-
275 ing (O'Connell & Chun, 2018) and as shown here during visual search (Fig. 2E). However, DeepM-
276 Reye goes beyond these earlier reports in multiple ways. Most importantly, earlier approaches
277 such as predictive-eye-estimation-regression (PEER, Son et al., 2020) required calibration data for
278 every single participant, meaning that at least two calibration scans need to be acquired during
279 each scanning session. In contrast, our deep-learning based approach generalizes across partici-
280 pants, allowing to perform eye tracking even when training and test labels are missing. The model
281 could be trained on the data of a few participants and then used for decoding from all other par-
282 ticipants. Moreover, earlier approaches were limited to the sampling resolution of the imaging
283 protocol, meaning that one average gaze position per functional image could be extracted. In con-
284 trast, we extracted gaze position at a moderate sub-TR resolution (~3Hz) and with higher accuracy
285 than previous approaches, allowing to perform MR-based eye tracking with a higher level of detail.
286 Third, as a proof-of-principle, we show that our model reconstructs viewing behavior even when
287 the eyes are closed. Finally, we provide the first open source and user-friendly implementation
288 for MR-based eye tracking as an interactive decoding pipeline inspired by other fMRI open source
289 initiatives (e.g. (Esteban et al., 2019)). DeepMReye hence overcomes several critical limitations of
290 earlier work, presenting the most general and versatile solution to camera-less eye tracking in MRI
291 to date.

292 What information does the model use?

293 Eye movements naturally entail movements of the eyeballs but also of the optic nerves and the
294 fatty tissue around them. To capture these movements, our custom eye masks cover a large area
295 behind the eyes excluding skull and brain tissue. When the eyes move, the multi-voxel-pattern in

296 these masks changes drastically (Fig. 1B), an effect that might be even amplified by the magnetic
297 field distortions often occurring around the eyes. DeepMReye hence likely utilizes information tra-
298 ditionally considered to be motion artifacts, which are not corrected by classical realignment during
299 preprocessing (Fig. S9, Fig. S10). The fact that the actual motion of the eye is used for decoding
300 also means that no hemodynamic lag needs to be considered (Fig. 2E). The current gaze position is
301 decoded directly from each TR respectively. We believe that two sources of information further con-
302 tribute to the moderate sub-imaging decoding resolution that we observed. First, different imaging
303 slices are being acquired at a different time within each TR and thus inherently carry some sub-TR
304 information. This is true also for fMRI protocols that use multiband acquisition, which includes
305 all datasets tested here. Future studies could examine the effect of slice timing on the decoding
306 resolution in more detail. Second, similar to motion blur in a long-exposure camera picture, the
307 MR-signal intensity of a voxel can itself be affected by movements. The multi-voxel-pattern at each
308 TR might hence reflect how much the eyes moved, and the same average gaze position might look
309 different depending on which positions were sampled overall within the respective TR.

310 **Looking forward**

311 DeepMReye offers a multitude of exciting applications ranging from simple behavioral monitor-
312 ing over confound removal to new and improved task-based analyses. Most basically, it offers an
313 additional and low-effort behavioral read-out for any fMRI-experiment and allows to monitor task
314 compliance for example by verifying that a fixation cross was fixated. Removing samples at which
315 fixation was not maintained from subsequent analysis has been shown to improve predictive mod-
316 eling results (LaConte & Glielmi, 2006) and may help to reduce the effects of in-scanner sleep more
317 easily (Tagliazucchi & Laufs, 2014).

318 Our approach enables studies of the relationship between viewing and brain activity, and may more
319 generally be used to inform almost any type of task-based model about the underlying viewing
320 behavior. This could for example further improve the explanatory power of predictive models
321 (Naselaris et al., 2011; Kriegeskorte & Douglas, 2019), and be especially promising for naturalistic
322 free-viewing paradigms because the currently attended aspect of a stimulus can be taken into
323 account (Sonkusare et al., 2019).

324 Importantly, eye movements can also be a major source of confounds in neuroimaging studies.
325 As mentioned in the introduction, if differences in viewing between two conditions remain unde-
326 tected, the interpretation of neuroimaging results may be compromised. We demonstrated here
327 that many brain regions are affected by this issue, many of which are not typically studied in the
328 context of eye movements (Fig. 4). Moreover, eye movements are associated with imaging artifacts
329 that can affect data integrity throughout the brain (McNabb et al., 2020). A popular way of minimiz-
330 ing such confounds is having participants fixate at a fixation cross, which is helpful but also puts
331 artificial constraints on a behavior that is fundamental to how we explore the world. Moreover, task
332 compliance cannot always be guaranteed. DeepMReye may allow to identify and potentially com-
333 pensate such confounds and artifacts for example by adding eye movement regressors directly to
334 a GLM analysis as it is standard practice for head-motion regressors. This promises to improve the
335 interpretability of task-based and resting-state fMRI results alike because nuisance variance would
336 no longer be assigned to the regressors of interest (Murphy et al., 2013).

337 Thus, DeepMReye can provide many experimental and analytical benefits that traditional eye-tracking
338 systems can provide too. Critically, it does so without any expensive equipment, trained staff or
339 experimental time to be used. It can therefore be used widely in both research and clinical settings

340 for example to study or diagnose neurodegenerative disorders (Anderson & MacAskill, 2013). Excit-
341 ingly, it can even go beyond traditional eye tracking in certain aspects, offering new experimental
342 possibilities that cannot easily be realized with a camera. For example, eye movements can be
343 tracked even while the eyes are closed, suggesting it could be used to study oculomotor systems in
344 the total absence of visual confounds, during resting state, and potentially even during rapid eye
345 movements (REM) sleep. Moreover, the across-participant generalization enables new studies of
346 patient groups for which camera-based eye trackers are not applicable. For example, DeepMReye
347 could be trained on data of healthy volunteers and then tested on visually impaired participants for
348 whom camera-based eye trackers cannot be calibrated. Most importantly, it allows gaze decoding
349 in already existing task-based and resting-state fMRI datasets, in principle including all datasets
350 that comprise the eyeballs. It could hence make new use of a large, existing and instantly available
351 data resource (see "User recommendations").

352 Finally, the same model architecture can be used to decode gaze position not only from the eyeballs
353 but also from brain activity directly. Doing so is as simple as replacing the eye masks by a regions-of-
354 interest mask of a certain brain region and accounting for the hemodynamic lag. We demonstrated
355 this possibility using fMRI data from area V1 (Fig. 2E). Likewise, the same decoding pipeline could
356 be used to decode other behavioral or stimulus features from brain activity, again showing the
357 power of deep-learning-based methods for image analysis and neuroscience in general (Frey et al.,
358 2019; Shen et al., 2017).

359 Limitations

360 It is important to note that DeepMReye also has certain limitations and disadvantages compared to
361 camera-based eye tracking. First, the eyeballs need to be included in the MRI images. This may not
362 always be possible and can affect the artifacts that eye movements can induce. In practice, how-
363 ever, many existing and future datasets do include the eyes, and even if not, DeepMReye could still
364 be used to decode from brain activity directly. Second, despite decoding at a temporal resolution
365 that is higher than the one of the underlying imaging protocol, our approach does by no means
366 reach the temporal resolution of a camera. Many aspects of viewing behavior happen on a time
367 scale that can hence not be studied with DeepMReye. For experiments requiring such high tem-
368 poral resolution, for example for studying individual saccades, we therefore recommend a camera
369 system. However, many fMRI studies will not require monitoring gaze at high temporal resolution.
370 This is because the regression analyses that are most commonly used in neuroimaging require the
371 eye-tracking data to be downsampled to the imaging resolution irrespective of the sampling rate
372 at which they were recorded. This means that even if gaze behavior was monitored at 1000 Hz with
373 a camera, the effective eye-tracking data resolution that enters the fMRI analysis is often the same
374 as the one of DeepMReye. Also, many MRI facilities simply do not have an MR-compatible camera,
375 leaving MR-based eye tracking as the only available option.

376 Conclusions

377 In sum, DeepMReye is a camera-less deep-learning based eye tracking framework for fMRI experi-
378 ments. It works robustly across a broad range of gaze behaviors and imaging protocols, allowing to
379 reconstruct viewing behavior with high precision even in existing datasets. This work emphasizes
380 the importance and the potential of combining eye tracking and neuroimaging for studying hu-
381 man brain function and provides a user-friendly and open source software solution that is widely
382 applicable post-hoc.

383 **Author Contributions**

384 MF & MN conceptualized the present work, developed the decoding pipeline and analyzed the data with input from CFD. MF wrote
385 the key model implementation code with help from MN. MN acquired most and analyzed all datasets, visualized the results and wrote
386 the manuscript with help from MF. MF, MN and CFD discussed the results & contributed to the manuscript.

387 **Declaration of interest**

388 The authors declare no conflicts of interest.

389 **Data and code availability**

390 Upon publication, we will share online our model code, documentation and Colab notebooks as well as eye-tracking calibration scripts
391 that can be used to acquire training data for DeepMReye. In addition, we share our pre-trained model weights estimated on all datasets
392 used in the present work. These model weights allow decoding viewing behavior without re-training the model in certain scenarios
393 (see "User recommendation" section for details). All shared code will be available here: <https://github.com/CYHSM/DeepMReye>.

394 **Acknowledgements**

395 We thank Ignacio Polti, Joshua B. Julian, Russell Epstein and Andreas Bartels for providing imaging and eye-tracking data that was
396 used in the present work. We further thank Caswell Barry for helpful discussions and Joshua B. Julian and Christopher I. Baker for
397 comments on an earlier version of this manuscript. This work is supported by the European Research Council (ERC-CoG GEOCOG
398 724836). CFD's research is further supported by the Max Planck Society, the Kavli Foundation, the Centre of Excellence scheme of the
399 Research Council of Norway – Centre for Neural Computation (223262/F50), The Egil and Pauline Braathen and Fred Kavli Centre for
400 Cortical Microcircuits and the National Infrastructure scheme of the Research Council of Norway - NORBRAIN (197467/F50).

401 References

- 402 Alexander, L. M., Escalera, J., Ai, L., Andreotti, C., Febre, K., Mangone, A., ... Milham, M. P. (2017). Data Descriptor: An open resource
403 for transdiagnostic research in pediatric mental health and learning disorders. *Scientific Data*, 4(1). doi: 10.1038/sdata.2017.181
- 404 Anderson, T. J., & MacAskill, M. R. (2013). Eye movements in patients with neurodegenerative disorders. *Nature Reviews Neurology*,
405 9(2), 74–85. doi: 10.1038/nrneurol.2012.273
- 406 Beauchamp, M. S. (2003). Detection of eye movements from fMRI data. *Magnetic Resonance in Medicine*, 49(2), 376–380. doi: 10.1002/
407 mrm.10345
- 408 Berman, R. A., Colby, C. L., Genovese, C. R., Voyvodic, J. T., Luna, B., Thulborn, K. R., & Sweeney, J. A. (1999). Cortical networks
409 subserving pursuit and saccadic eye movements in humans: An FMRI study. *Human Brain Mapping*, 8(4), 209–225. doi: 10.1002/
410 (SICI)1097-0193(1999)8:4<209::AID-HBM5>3.0.CO;2-0
- 411 Biewald, L. (2020). *Experiment Tracking with Weights Biases* (Nos. 1–5).
- 412 Brodoehl, S., Witte, O. W., & Klingner, C. M. (2016). Measuring eye states in functional MRI. *BMC Neuroscience*, 17(1). doi: 10.1186/
413 s12868-016-0282-7
- 414 Duchowski, A. T. (2017). *Eye tracking methodology: Theory and practice: Third edition*. Cham: Springer International Publishing. doi:
415 10.1007/978-3-319-57883-5
- 416 Ehinger, K. A., Hidalgo-Sotelo, B., Torralba, A., & Oliva, A. (2009). Modelling search for people in 900 scenes: A combined source model
417 of eye guidance. *Visual cognition*, 17(6–7), 945–978. doi: 10.1080/13506280902834720
- 418 Esteban, O., Markiewicz, C. J., Blair, R. W., Moodie, C. A., Isik, A. I., Erramuzpe, A., ... others (2019). fmriprep: a robust preprocessing
419 pipeline for functional mri. *Nature methods*, 16(1), 111–116. doi: 10.1038/s41592-018-0235-4
- 420 Franceschiello, B., Di Sopra, L., Minier, A., Ionta, S., Zeugin, D., Notter, M. P., ... Murray, M. M. (2020). 3-Dimensional magnetic
421 resonance imaging of the freely moving human eye. *Progress in Neurobiology*, 101885. doi: 10.1016/j.pneurobio.2020.101885
- 422 Frey, M., Tanni, S., Perrodin, C., O’Leary, A., Nau, M., Kelly, J., ... Barry, C. (2019). *Deepinsight: a general framework for interpreting*
423 *wide-band neural activity* (preprint). Neuroscience. doi: 10.1101/871848
- 424 Hebart, M. N., Dickter, A. H., Kidder, A., Kwok, W. Y., Corriveau, A., Van Wicklin, C., & Baker, C. I. (2019). THINGS: A database of 1,854
425 object concepts and more than 26,000 naturalistic object images. *PLoS ONE*, 14(10), e0223792. doi: 10.1371/journal.pone.0223792
- 426 Heberlein, K., Hu, X., Peltier, S., & LaConte, S. (2006). Predictive Eye Estimation Regression (PEER) for Simultaneous Eye Tracking and
427 fMRI. *Proceedings 14th Scientific Meeting, International Society for Magnetic Resonance in Medicine*, 14, 2808.
- 428 Julian, J. B., Keinath, A. T., Frazzetta, G., & Epstein, R. A. (2018). Human entorhinal cortex represents visual space using a boundary-
429 anchored grid. *Nature Neuroscience*, 21(2), 191–194. doi: 10.1038/s41593-017-0049-1
- 430 Kafkas, A., & Montaldi, D. (2011). Recognition memory strength is predicted by pupillary responses at encoding while fixation patterns
431 distinguish recollection from familiarity. *Quarterly Journal of Experimental Psychology*, 64(10), 1971–1989. doi: 10.1080/17470218
432 .2011.588335
- 433 Keck, I. R., Fischer, V., G.puntonet, C., & Lang, E. W. (2009). Eye movement quantification in functional mri data by spatial independent
434 component analysis. In T. Adali, C. Jutten, J. M. T. Romano, & A. K. Barros (Eds.), *Lecture notes in computer science (including subseries*
435 *lecture notes in artificial intelligence and lecture notes in bioinformatics)* (Vol. 5441, pp. 435–442). Berlin, Heidelberg: Springer Berlin
436 Heidelberg. doi: 10.1007/978-3-642-00599-2_55
- 437 Kingma, D. P., & Ba, J. L. (2015). Adam: A method for stochastic optimization. *3rd International Conference on Learning Representations*,
438 *ICLR 2015 - Conference Track Proceedings*.
- 439 Kriegeskorte, N., & Douglas, P. K. (2019). Interpreting encoding and decoding models. *Current Opinion in Neurobiology*, 55, 167–179.
440 doi: 10.1016/j.conb.2019.04.002
- 441 LaConte, S. M., & Glielmi, C. B. (2006). Verifying visual fixation to improve fMRI with predictive eye estimation regression (PEER).
442 *NeuroImage*, 50183.
- 443 Liu, Z. X., Shen, K., Olsen, R. K., & Ryan, J. D. (2017). Visual sampling predicts hippocampal activity. *Journal of Neuroscience*, 37(3),
444 599–609. doi: 10.1523/JNEUROSCI.2610-16.2016
- 445 McNabb, C. B., Lindner, M., Shen, S., Burgess, L. G., Murayama, K., & Johnstone, T. (2020). Inter-slice leakage and intra-slice aliasing in
446 simultaneous multi-slice echo-planar images. *Brain Structure and Function*, 225(3), 1153–1158. doi: 10.1007/s00429-020-02053-2
- 447 Misra, D. (2019). Mish: A self regularized non-monotonic neural activation function. *arXiv preprint arXiv:1908.08681*.
- 448 Morrone, M. C., Ross, J., & Burr, D. (2005). Saccadic eye movements cause compression of time as well as space. *Nature Neuroscience*,
449 8(7), 950–954. doi: 10.1038/nn1488
- 450 Murphy, K., Birn, R. M., & Bandettini, P. A. (2013). Resting-state fMRI confounds and cleanup. *NeuroImage*, 80, 349–359. doi: 10.1016/
451 j.neuroimage.2013.04.001
- 452 Nau, M., Navarro Schröder, T., Bellmund, J. L., & Doeller, C. F. (2018a). Hexadirectional coding of visual space in human entorhinal
453 cortex. *Nature Neuroscience*, 21(2), 188–190. doi: 10.1038/s41593-017-0050-8

- 454 Nau, M., Schindler, A., & Bartels, A. (2018b). Real-motion signals in human early visual cortex. *NeuroImage*, *175*, 379–387. doi:
455 10.1016/j.neuroimage.2018.04.012
- 456 Naselaris, T., Kay, K. N., Nishimoto, S., & Gallant, J. L. (2011). Encoding and decoding in fMRI. *NeuroImage*, *56*(2), 400–410. doi:
457 10.1016/j.neuroimage.2010.07.073
- 458 O’Connell, T. P., & Chun, M. M. (2018). Predicting eye movement patterns from fMRI responses to natural scenes. *Nature Communica-*
459 *tions*, *9*(1). doi: 10.1038/s41467-018-07471-9
- 460 Pedregosa, F., Varoquaux, G., Gramfort, A., Michel, V., Thirion, B., Grisel, O., ... Duchesnay, E. (2011). Scikit-learn: Machine Learning
461 in Python. *Journal of Machine Learning Research*, *12*, 2825–2830.
- 462 Petit, L., & Haxby, J. V. (1999). Functional anatomy of pursuit eye movements in humans as revealed by fMRI. *Journal of Neurophysiology*,
463 *82*(1), 463–471. doi: 10.1152/jn.1999.82.1.463
- 464 Sathian, K., Lacey, S., Stilla, R., Gibson, G. O., Deshpande, G., Hu, X., ... Glielmi, C. (2011). Dual pathways for haptic and visual perception
465 of spatial and texture information. *NeuroImage*, *57*(2), 462–475. doi: 10.1016/j.neuroimage.2011.05.001
- 466 Shen, D., Wu, G., & Suk, H. I. (2017). Deep Learning in Medical Image Analysis. *Annual Review of Biomedical Engineering*, *19*(1), 221–248.
467 doi: 10.1146/annurev-bioeng-071516-044442
- 468 Son, J., Ai, L., Lim, R., Xu, T., Colcombe, S., Franco, A. R., ... Milham, M. (2020). Evaluating fMRI-Based Estimation of Eye Gaze during
469 Naturalistic Viewing. *Cerebral Cortex*, *30*(3), 1171–1184. doi: 10.1093/cercor/bhz157
- 470 Sonkusare, S., Breakspear, M., & Guo, C. (2019). Naturalistic Stimuli in Neuroscience: Critically Acclaimed. *Trends in Cognitive Sciences*,
471 *23*(8), 699–714. doi: 10.1016/j.tics.2019.05.004
- 472 Tagliazucchi, E., & Laufs, H. (2014). Decoding Wakefulness Levels from Typical fMRI Resting-State Data Reveals Reliable Drifts between
473 Wakefulness and Sleep. *Neuron*, *82*(3), 695–708. doi: 10.1016/j.neuron.2014.03.020
- 474 Tregellas, J. R., Tanabe, J. L., Miller, D. E., & Freedman, R. (2002). Monitoring eye movements during fMRI tasks with echo planar images.
475 *Human Brain Mapping*, *17*(4), 237–243. doi: 10.1002/hbm.10070
- 476 Voss, J. L., Bridge, D. J., Cohen, N. J., & Walker, J. A. (2017). A Closer Look at the Hippocampus and Memory. *Trends in Cognitive Sciences*,
477 *21*(8), 577–588. doi: 10.1016/j.tics.2017.05.008
- 478 Wagner, A. D., Schacter, D. L., Rotte, M., Koutstaal, W., Maril, A., Dale, A. M., ... Buckner, R. L. (1998). Building memories: remembering
479 and forgetting of verbal experiences as predicted by brain activity. *Science*, *281*(5380), 1188–1191. doi: 10.1126/science.281.5380
480 .1188
- 481 Wolfe, J. M. (2020). Visual Search: How Do We Find What We Are Looking For? *Annual Review of Vision Science*, *6*(1). doi: 10.1146/
482 annurev-vision-091718-015048

483 User recommendations

484 General recommendations: Despite successfully applying DeepMReye to data obtained with 14 scanning protocols, our datasets still
485 capture only a limited number of sequence parameters and behaviors. We therefore generally recommend running a pilot study using
486 the setup and the imaging protocol that was or will be used in the acquisition of the to-be-analyzed dataset. The larger the sample
487 size used for model training, the more data is being acquired for each participant, and the more similar the viewing behavior is to the
488 one of the test set, the better the decoding will be.

489 We further recommend thinking about whether the dataset includes at least some moments at which ground truth positions are
490 known. For future studies, such scenarios could be added by design to validate the decoding output later on e.g. by presenting a
491 fixation cross at various locations on the screen in the course of scanning. If the viewing behavior in the test set is unknown, we
492 recommend training the model on a mixture of smooth pursuit and fixation with variable duration while sampling as many screen
493 locations as possible.

494 To ensure that the eye masks fit every participant, the input data is being warped into our own functional MNI group template space.
495 Many popular normalization algorithms rely on brain tissue segmentation for normalization and hence typically neglect the eyeballs.
496 We therefore recommend users to apply non-linear warping algorithms that are agnostic to the underlying tissue. Here, we used the
497 Advanced Normalization Tools (ANTs) running under Python.

498 Note that the placement of the mirror inside the MRI has a large impact on the position of the eyeballs relative to the screen. Even if
499 participants fixate at the same position on the screen, depending on the mirror placement the eyeballs might be oriented differently.
500 Our three-step co-registration procedure of the eyes mitigates this problem, but we still recommend users who acquire new data to
501 place the mirror at approximately the same location and angle for all participants.

502 For users wishing to perform eye tracking while the eyes are closed, we recommend training the model on a combination of eyes-
503 closed and eyes-open gaze labels. One option to obtain such labels would be to have participants fixate at various target locations
504 on the screen and then close their eyes without moving them for 2-3 s. For studies planning on using DeepMReye during in-scanner
505 sleep, we further recommend adding an awake but eyes-closed validation paradigm to the study, which could be similar to the one
506 used here (Fig. 3B).

507 Finally, irrespective of which of the following decoding option is used, we recommend assessing the predicted error scores carefully
508 for each participant (Fig. 2B, Fig. S1). The predicted error score is tightly correlated with the Euclidean error between real and decoded
509 gaze position and hence allows to detect and remove outliers even when test labels are missing.

510 In the following, we outline multiple ways of how DeepMReye can be used. Which option is best depends on how much experimental
511 time and data are available.

512 User option 1: To maximize accuracy and robustness, we recommend users who acquire new data to scan a short calibration paradigm
513 in addition to their regular experimental paradigm. This could be as simple as presenting various fixation targets sequentially at
514 different locations on the screen (see e.g. dataset 1). Upon publication, we will provide the code for such a calibration scan online
515 (see 'Data & code availability' statement). Importantly, the more similar the viewing behavior is between training and test set the more
516 accurate the decoding will be. Acquiring such calibration data will allow training the model on data acquired in the same participants
517 with the same fMRI sequence that the model is being tested on, which promises the best result. This option is recommended in
518 any case, but especially when eyes-closed data are being analyzed. Note that in this case the model is still evaluated on data of all
519 participants, with the calibration data used for model training and the actual experimental data used for decoding.

520 User option 2: For users who cannot scan individual eye tracking calibrations for all participant, we recommend acquiring such cali-
521 bration data at least for a subset of participants for example during piloting. This will allow training the model on some participants
522 scanned on the same MRI scanner with the same imaging protocol, and then decode from others. This also offers a solution for already
523 existing datasets. In this case, we again recommend scanning calibration data for a few participants with the same imaging protocol
524 on the same MRI scanner if possible. We suggest acquiring calibration data for at least 6-8 participants, and to carefully evaluate the
525 model performance within the training set. If necessary, more participants can be added. In addition, stronger dropout regularization
526 and/or the use of ensemble learning with various dropout strengths can help to improve model training in case of small sample sizes.

527 User option 3: If no new calibration data can be acquired, users may use an already pre-trained version of DeepMReye that we provide.
528 Note that we did show that our model generalizes across datasets, but also that it performed less accurately than the across-participant
529 prediction within each dataset. We therefore recommend this option only for datasets in which at least some ground-truth-validation
530 labels are known. Having said that, if more training data are being added to the model training in the future, the across-dataset
531 prediction is expected to further improve. Especially important will be data featuring even more diverse viewing behaviors and imaging
532 protocols.

533 Methods

534 Datasets

535 DeepMRye was trained and tested on data of 268 participants acquired on five 3T MRI scanners with 14 different scanning protocols
 536 and various pre-processing settings. The individual datasets are described below and were partially used in earlier reports. For other
 537 details of each individual dataset please see the original published articles (Alexander et al., 2017; Nau et al., 2018a, 2018b; Julian et
 538 al., 2018). A T1-weighted structural scan with 1 mm isotropic voxel resolution was acquired for all participants, and camera-based
 539 eye-tracking data was included for participants in datasets 3-6. An overview of the datasets is provided in Table 1.

Dataset	Behavior	TR	Voxel size	Participants	#TRs	#Minutes	Gaze labels	Field of View
1	Fixation	800ms	2.4mm ³	n = 170	270	3.60	Target	19° x 15°
2	Pursuit	1000ms	2.0mm ³	n = 24	3961	66.01	Both	15° x 15°
3	Pursuit	1020ms	2.0mm ³	n = 34	3568	60.65	Both	10° x 10°
4	Pursuit	870ms	2.0mm ³	n = 9	2778	40.28	Target	8° x 8°
5	Free viewing	1000ms	2.0mm ³	n = 27	2128	35.46	Camera	17° x 17°
		1250ms	1.5mm ³		287			
		1800ms	1.5mm ³		200			
		2500ms	1.5mm ³		144			
		1250ms	2.0mm ³		287			
6	All the above	1800ms	2.0mm ³	n = 4	200	~ 6	Both	30° x 15°
		2500ms	2.0mm ³		144			
		1250ms	2.5mm ³		287			
		1800ms	2.5mm ³		199			
		2500ms	2.5mm ³		144			

Table 1: Overview of the six datasets. We list the dataset number, the viewing behavior that was tested, the repetition time (TR) and voxel size of the imaging protocol, the number of participants, the amount of data acquired for each participant expressed as the average number of acquired volumes (#TRs) and as the total scanning time (#Minutes), the type of gaze labels that DeepMRye was trained and tested on (incl. camera-based labels, screen coordinates of the fixation target, or both) as well as the task-relevant field of view (FoV) of the participant.

540 Dataset 1: Fixation and saccades

541 Data & task: These data were made publicly available by Alexander and colleagues (Alexander et al., 2017) and were downloaded from
 542 the Healthy Brain Network (HBN) Biobank (http://fcon_1000.projects.nitrc.org). These data were also used in earlier reports (Son et al.,
 543 2020). It is part of a larger and ongoing data collection effort with pediatric focus and comprises participants between 5 and 21 years of
 544 age. We limited our analysis to a subset of the full dataset for which we ensured that there were no visible motion artifacts in either the
 545 T1- or the average T2*-weighted images and the eyeballs were fully included in the functional images. We included 170 participants
 546 in total. For each participant, at least two fMRI runs were scanned in which they performed a typical eye tracking calibration protocol.
 547 In each run, they fixated at a fixation target that sequentially moved through 27 locations on the screen, with each location being
 548 sampled twice for 5s. Gaze positions were sampled within a window of X = 19° and Y = 15° visual angle. The screen coordinates of the
 549 fixation target served as training and testing labels for the main analyses (Fig. 2).

550 fMRI-data acquisition & preprocessing: Imaging data were acquired on a Siemens 3T Tim Trio MRI scanner located at the Rutgers
 551 University Brain Imaging Center, Newark, USA. Following EPI parameters were used: voxel size = 2.4mm isotropic, TR = 800ms, TE =
 552 30ms, flip angle = 31°, multiband factor = 6. Images were coregistered to our template space as described below.

553 Dataset 2: Smooth pursuit 1

554 Data & task: These data were used in one of our previous reports (Nau et al., 2018b). Nine participants performed a smooth pursuit
 555 visual tracking task in which they either tracked a fixation target moving on a circular trajectory with a radius of 8° visual angle or
 556 one that remained at the screen center. In addition, planar-dot-motion stimuli were displayed in the background moving on the
 557 same circular trajectory at various speeds. This resulted in a total of 9 different conditions. Following pursuit and motion speed
 558 combinations were tested in separate trials: [eye, background in °/s] = [0,0], [0,1], [0,3], [2,1], [2,2], [2,3], [3,2], [3,3], [3,4]. These
 559 conditions were tested in blocks of 12 seconds in the course of 34 trials over 4 scanning runs of ~10.5 minutes each. To balance
 560 attention across conditions, participants performed a letter-repetition-detection task displayed on the fixation target. Gaze positions
 561 were sampled within a window of X = 8° and Y = 8° visual angle. The screen coordinates of the fixation target served as training and
 562 testing labels for our model.

563 fMRI-data acquisition & preprocessing: Imaging data were acquired on a Siemens 3T MAGNETOM Prisma MRI scanner located at
 564 the Max-Planck-Institute for Biological Cybernetics in Tuebingen, Germany. Following EPI-parameters were used: voxel size = 2mm
 565 isotropic, TR = 870ms, TE = 30ms, flip angle = 56°, multiband factor = 4, GRAPPA factor = 2. Note that 9 other participants were
 566 excluded because the functional images did not or only partially included the eyeballs. Images were corrected for head motion and
 567 field distortions using SPM12 (www.fil.ion.ucl.ac.uk/spm/) and then coregistered to our template space as described below.

568 **Eye tracking:** We monitored gaze position at 60 Hz using a camera-based eye tracker by Arrington Research. Please note that these
569 eye-tracking data showed a higher noise level than the other datasets due to drift and because the pupil was frequently lost. We
570 therefore used the screen coordinates of the fixation target for model training and testing as in dataset 1. To still visually compare the
571 decoding output to the eye-tracking data post-hoc, we removed blinks, detrended the eye tracking time series using a second-order
572 polynomial function and median-centered it on the screen center. We removed samples in which the pupil was lost by limiting the
573 time series to the central 14x14 degree visual angle, smoothed it using a running-average kernel of 100ms and scaled it to match the
574 data range of the fixation target using the sum-of-squared-errors as loss function. The time series was then split into the individual
575 scanning acquisitions.

576 **Dataset 3: Smooth pursuit 2**

577 **Data & task:** These data are currently being analyzed for another report and comprised 34 participants (Polti & Nau et al., in prep).
578 Like in dataset 2, participants performed a smooth pursuit visual tracking task in which they fixated at a fixation target moving on a
579 star-shaped trajectory. Twenty-four eye movement directions were sampled in steps of 15° at four speed levels: 4.2°/s, 5.8°/s, 7.5°/s
580 and 9.1°/s. Speeds were interleaved and sampled in a counterbalanced fashion. In addition to the visual tracking task, participants
581 performed a time-to-collision (TTC) task. The trajectory was surrounded by a circular yellow line on gray background with a radius of
582 10° visual angle centered on the screen center. Whenever the fixation target stopped moving before switching direction, participants
583 indicated by button press when the target would have touched the yellow line if it continued moving. Gaze positions were sampled
584 within a window of X = 10° and Y = 10° visual angle. Each participant performed a total of 768 trials in the course of 4 scanning runs
585 with 16-18 minutes (including a short break in the middle). The screen coordinates of the fixation target served as training and testing
586 labels for the main analyses (Fig. 2).

587 **fMRI-data acquisition & preprocessing:** Imaging data were acquired on a Siemens 3T MAGNETOM Skyra located at the St. Olavs
588 Hospital in Trondheim, Norway. Following EPI-parameters were used: voxel size = 2mm isotropic, TR = 1020ms, TE = 34.6ms, flip
589 angle = 55°, multiband factor = 6. Images were corrected for head motion using SPM12. The FSL topup function was used to
590 correct field distortions using an image acquired with the same protocol except that the phase-encoding direction was inverted
591 (<https://fsl.fmrib.ox.ac.uk/fsl/fslwiki/topup>). Images were then coregistered to our template space as described below.

592 **Eye tracking:** We monitored gaze position during the experiment at a rate of 1000 Hz using an MR-compatible infrared-based eye
593 tracker (Eyelink1000). Blinks were removed, the time series was downsampled to 100hz, linearly detrended within each scanning run
594 and smoothed with a running-average kernel of 100ms. We then split the time series into individual scanning acquisitions (TR's) to
595 obtain the final training and testing gaze labels for our model. The camera-based eye tracking labels served as training and testing
596 labels for supplementary analyses (Fig. S5).

597 **Dataset 4: Smooth pursuit 3**

598 **Data & task:** These data were used in one of our previous reports (Nau et al., 2018a). Twenty-four participants performed a smooth
599 pursuit visual tracking task in which they tracked a fixation target moving at a speed of 7.5°/s on a star-shaped trajectory with 36
600 directions. The target moved within a virtual arena which participants oversaw from bird's eye view. Eye movement directions were
601 sampled in steps of 10°. In a visual-motion control condition, the target remained at the screen center and the arena moved instead.
602 Participants additionally performed a spatial memory task. They memorized the location of colored objects on the screen, which were
603 shown only when the fixation target moved across them. Gaze positions were sampled within a window of X = 15° and Y = 15° visual
604 angle. Each participant performed a total of 81 trials in the course of 9 scanning runs. This included 54 smooth pursuit trials of 60
605 seconds each and 27 center fixation trials of 30 seconds each. The screen coordinates of the fixation target served as training and
606 testing labels for the main analyses (Fig. 2).

607 **fMRI-data acquisition & preprocessing:** Imaging data were acquired on a Siemens 3T MAGNETOM PrismaFit MRI scanner located at
608 the Donders Centre for Cognitive Neuroimaging, Nijmegen, the Netherlands. Following EPI-parameters were used: voxel size = 2mm
609 isotropic, TR = 1000ms, TE = 34ms, flip angle = 60°, multiband factor = 6. Data were realigned using SPM12 (www.fil.ion.ucl.ac.uk/spm/)
610 and coregistered to our template space as described below.

611 **Eye tracking:** Similar to dataset 3, we again monitored gaze position during the experiment at 1000 Hz using an Eyelink 1000 eye
612 tracker. Blinks were removed and the data were downsampled to the monitor refresh rate of 60hz. We then reduced additional
613 tracking noise by removing samples at which the pupil size diverged more than one standard deviation from the mean, by removing
614 the inter-trial-interval during which most blinks occurred and by smoothing the time series with a running-average kernel of 100ms.
615 We then linearly detrended and median-centered the time series of each trial individually to remove drift. Finally, we split the time
616 series according to the underlying scanner acquisition times to create our final training and testing labels for this dataset. Note that
617 the original dataset (Nau et al., 2018a) comprises 5 additional participants for which no eye-tracking data has been obtained and that
618 were excluded. The camera-based eye tracking labels served as training and testing labels for supplementary analyses (Fig. S5).

619 **Dataset 5: Visual search**

620 **Data & task:** These data were kindly provided by Julian and colleagues (Julian et al., 2018). Twenty-seven participants performed a self-
621 paced visual search task, searching for the letter "L" in a search display filled with distractor letters "T". Upon detection, participants
622 pressed a button. Each trial lasted for an average of 7.50 seconds, followed by fixation at the screen center for 2 - 6 seconds. The
623 number of distractors varied over trials between 81, 100, 144, 169, or 121. Participants performed either 4 or 6 runs of 6.5 minutes
624 each. Task-relevant gaze positions were sampled within a window of X = 17° and Y = 17° visual angle. Camera-based eye-tracking data
625 were acquired and served as training and testing labels for our model (see below).

626 **fMRI-data acquisition & preprocessing:** Imaging data were acquired on a Siemens 3T MAGNETOM Prisma MRI scanner located at the
627 Center for Functional Imaging in Philadelphia, USA. Following EPI-parameters were used: voxel size = 2mm isotropic, TR = 1000ms, TE
628 = 25ms, flip angle = 45°, multiband factor = 4. Images were corrected for head motion using SPM12 and coregistered to our template
629 space as described below. Note that the original dataset includes 9 more participants whose eyeballs were cut off on the functional
630 images and that were excluded here.

631 **Eye tracking:** Gaze position was monitored at 30 Hz using the camera-based eye tracker LiveTrack AV by Cambridge Research Systems.
632 We median-centered the time series and removed tracking noise by limiting the time series to values within the central 40 x 40 visual
633 degree. We then split the data into individual scanning acquisitions to obtain the final gaze labels for model training and test.

634 **Dataset 6: Fixation, smooth pursuit, free viewing & eyes-closed eye movements**

635 **Data & task:** Four participants performed 4 viewing tasks while imaging data were acquired in the course of 9 scanning runs using
636 9 EPI-protocols (1 per run) along with concurrent camera-based eye tracking. First, they fixated sequentially at 37 locations on the
637 screen for 2s each starting in the screen center. The locations were determined using a custom random-walk algorithm that balanced
638 the sampling of 12 directions (30 steps) and distances between the fixation points (4, 8, or 12 visual angle). Next, they performed a
639 smooth pursuit version of this random-walk task for which we linearly interpolated the trajectory between fixation points. This resulted
640 in a target moving sequentially into 12 directions at a speed of either 2/s, 4/s, or 6/s, changing to a randomly selected direction and
641 speed every 2s. Next, participants freely explored 30 sequentially presented images of everyday objects for 3s each. The images were
642 randomly drawn from the THINGS database (Hebart et al., 2019). Finally, participants closed their eyes and moved them either from
643 left to right or from top to bottom for a total of 105 s. Switches between horizontal and vertical movements were indicated via button
644 press.

645 **fMRI-data acquisition & preprocessing:** Imaging data were acquired using 9 EPI-sequences on a Siemens 3T MAGNETOM Skyra located
646 at the St. Olavs Hospital in Trondheim, Norway. The sequences featured 3 repetition times and 3 voxel sizes in a 3x3 design. All
647 images were corrected for head motion using SPM12 and coregistered to our template space as described below. See Table 2 for
648 parameter details. Data acquisition was approved by the regional committees for medical and health research ethics (REC), Norway,
649 and participants gave written informed consent prior to scanning.

Sequence	Voxel size	TR	TE	FA	MB	pF	#Slices
1	1.5mm ³	1250ms	26ms	66	4	7/8	40
2	1.5mm ³	1800ms	26ms	74	4	7/8	40
3	1.5mm ³	2500ms	26ms	80	4	7/8	40
4	2.0mm ³	1250ms	26ms	66	4	7/8	60
5	2.0mm ³	1800ms	26ms	74	4	7/8	60
6	2.0mm ³	2500ms	26ms	80	4	7/8	60
7	2.5mm ³	1250ms	26ms	66	4	7/8	60
8	2.5mm ³	1800ms	26ms	74	4	7/8	60
9	2.5mm ³	2500ms	26ms	80	4	7/8	60

Table 2: Sequence parameters of the 9 EPI-protocols used in the acquisition of dataset 6. For each sequence, we list the isotropic voxel size, the repetition time (TR), the echo time (TE), the flip angle (FA), the multiband factor (MB), partial Fourier factor (pF) and the number of slices (#Slices). All flip angles were aligned to the respective Ernst angle.

650 **Eye tracking:** Gaze position was monitored during the experiment at 1000 Hz using an Eyelink 1000 eye tracker. Tracking noise was
651 reduced by excluding samples at which the pupil size diverged more than two standard deviations from the mean. Blinks were
652 removed. The time series was downsampled to 60 Hz and median-centered based on the median gaze position of the free viewing
653 condition within each scanning run. We then split the time series into individual scanning acquisitions to obtain the final training and
654 testing gaze labels for our model.

655 **Eye masks, co-registration & normalization**

656 Eye masks were created by manually segmenting the eyeballs including the adjacent optic nerve, fatty tissue and muscle area in
657 the Colin27 structural MNI template using itkSNAP (<http://www.itksnap.org>, Fig. 1A). We then created a group-average functional
658 template by averaging the co-registered functional images of 29 participants. These were acquired while the participants fixated at
659 the screen center for around 13 minutes each in the course of a longer scanning session (Nau et al., 2018a). To ensure that the
660 final eye masks contain the eyeballs of every participant, all imaging data underwent three co-registration steps conducted using
661 Advanced Normalization Tools (ANTs) within Python (ANTsPy). First, we co-registered each participant's mean-EPI non-linearly to our
662 group-level average template. Second, we co-registered all voxels within a bounding box that included the eyes to a pre-selected
663 bounding box in our group template to further improve the fit. Finally, we co-registered the eyeballs to the ones of the template
664 specifically. Importantly, all data in our group-average template reflected gaze coordinates (0,0), i.e. the screen center. This third
665 eyeball co-registration hence centered the average gaze position of each participant on the screen. We did this to improve the fit but
666 also because it aligned the orientation of the eyeballs relative to the screen across participants. Finally, each voxel underwent two

667 normalization steps. First, we subtracted the across-run median signal intensity from each voxel and sample and divided it by the
668 median absolute deviation (MAD) over time (temporal normalization). Second, for each sample, we subtracted the mean across all
669 voxels within the eye masks and divided by the standard deviation across voxels (spatial normalization). The fully co-registered and
670 normalized voxels inside the eye masks served as model input.

671 Model architecture

672 DeepMReye is a convolutional neural network that uses three-dimensional data to classify a two-dimensional output; the horizontal
673 (X) and vertical (Y) gaze coordinates on the screen. The model uses the voxel intensities from the eye masks as input and passes
674 it through a series of 3D-convolutional layers interleaved with group normalization and non-linear activation functions (mish, [Misra](#)
675 [2019](#)). In detail, the eye mask (input layer) is connected to a 3D convolutional block with a kernel size of 3 and strides of 1, followed
676 by dropout and a 3D convolutional downsampling block which consists of one 3D-convolution followed by a 2x2x2 average pooling
677 layer. After this layer, we use a total of six residuals blocks, in which the residual connection consists of one 3D convolutional block,
678 concatenated via simple addition. Each residual block consists of group normalization, non-linear activation, and a 3D convolution,
679 which is applied twice before being added to the residual connection. This results in a bottleneck layer consisting of 7680 units, which
680 we resample to achieve sub-TR resolution (see details below). The time resolution dictates the number of resampled bottleneck layers,
681 with e.g. 10 resampled layers producing a 10 times higher virtual resolution than the original TR. Each resampled layer is connected
682 to a dense (fully-connected) layer which decodes the corresponding gaze position.

683 In addition to the above described model decoding gaze position directly, we also added a second block of fully-connected layers
684 connected to the bottleneck layer. This second fully-connected layer block did not classify gaze position, but instead tried to predict
685 the Euclidean error of the first model. This allowed us to obtain an unsupervised Euclidean error for each decoded gaze sample, even
686 when test labels were missing. We refer to this predicted, unsupervised Euclidean error as the predicted error. It indicates how certain
687 the model is about its own gaze decoding output and is strongly correlated with the real Euclidean error in our test data (Fig. 2B, Fig.
688 S1). If the unsupervised error is high, the model itself anticipates that the decoded gaze position likely diverges much from the real
689 gaze position. Accordingly, samples with high predicted error should not be trusted. DeepMReye is trained using a combination of
690 the two losses, the Euclidean Error (90% weighting) and the predicted error loss (10% weighting) as described in detail below.

691 Model optimization & training

692 Hyper-parameters were optimized using random search, which we monitored using the 'Weights & Biases' model tracking tool ([Biewald,](#)
693 [2020](#)). Following parameters were optimized: the learning rate (0.001-0.00001), the number of residual blocks (depth, 3-6), the size
694 of the filters (16-64), the filter multiplier per layer (1-2, e.g. 32, 64, 128 uses a multiplier of 2), the activation function (relu, elu, mish),
695 the number of groups in the group normalization (4,8,16), the number of fully-connected layers (1,2), the number of units in each
696 fully-connected layer (128-1024) as well as the dropout rate (0-0.5). In addition, to further improve the generalizability of our model,
697 we added following data augmentations to the model training: input scaling, translations (X, Y, Z) and rotations (azimuth, pitch, and
698 roll) which were applied on each sample.

699 We used Adam as learning algorithm ([Kingma & Ba, 2015](#)) and a batch size of 8 to train the model. Because considering samples from
700 different participants improved model performance in an earlier version of our pipeline, we mixed samples in each training batch
701 to represent 3D-inputs from different participants. For estimating the loss between real and predicted gaze position we used the
702 Euclidean error:

$$\mathcal{L}_{ED} = \sqrt{\sum_{i=1}^M (\hat{y}_i - y_i)^2} \quad (1)$$

703 with y_i the real gaze position, and \hat{y}_i the predicted gaze position. For calculating the predicted error, which reflects an unsupervised
704 estimate of the Euclidean error, we used the mean squared error between real and predicted Euclidean error, which itself has been
705 computed using the real and predicted gaze path as described above. The predicted error was computed as:

$$\mathcal{L}_{MSE} = \frac{1}{M} \sum_{i=1}^M (\hat{y}_i - y_i)^2 \quad (2)$$

706 with y_i being the Euclidean error between real and predicted gaze path (\mathcal{L}_{ED}), and \hat{y}_i being the predicted Euclidean error for this sample.
707 The full loss for optimizing the model weights was computed as:

$$\mathcal{L} = 0.1 * \mathcal{L}_{MSE} + \mathcal{L}_{ED} \quad (3)$$

708 Decoding schemes

709 We implemented three decoding schemes differing in how the data was split into training and test set. These decoding schemes are
710 described in the following.

711 Within-participant decoding: Here, we split the data of each participant into two equally sized partitions (50/50% split). The model was
712 trained on one half of the data of all participants and then tested on the other half of the data of all participants. This cross-validation

713 procedure allowed the model to learn about the intricacies and details of each participant's MR-signal and behaviors, while still having
714 to generalize across participants and to new data of the same participants (Fig. S4).

715 Across-participant decoding: To test whether the model generalizes to held-out and hence fully independent participants, we further
716 implemented an across-participant decoding scheme. This scheme represents our default pipeline and was used to obtain the main
717 results Fig. 2. Each dataset was split into 5 equally sized partitions containing different participants. We then trained the model on
718 4 of these data partitions and then decoded from the fifth (80/20% split). This procedure was cross-validated until all data partitions
719 and hence all participants were tested once. The across-participant decoding scheme requires the model to generalize to eyeballs
720 and behavioral priors that it has not encountered during training. The fMRI and eye-tracking data however have been acquired on
721 the same scanner and with the same scanning protocol.

722 Across-dataset decoding: Finally, we tested whether DeepMRye generalizes across datasets that have been acquired in independent
723 participants performing different viewing tasks scanned on different scanners and with different scanning protocols. We trained the
724 model in a leave-one-dataset-out fashion using all datasets (Fig. 2), meaning that the model was trained on all datasets except one
725 and then tested on the one that was held out. This procedure was cross-validated until all datasets and hence all participants were
726 tested once. Note that the voxel sizes and repetition times used for the acquisition of the key datasets 1-5 were similar, but that the
727 model still had to generalize across different participants, MRI scanners and other scan parameters (e.g. slice orientation). Further
728 note that the model performance of the across-dataset procedure would likely further improve if even more diverse viewing behaviors
729 and fMRI data were used for model training (Fig. S4).

730 **Model quantification**

731 To quantify model performance, we used the Euclidean error as described above for model training and evaluation. In addition, we
732 computed the Pearson correlation and the R^2 -score as implemented in scikit-learn (Pedregosa et al., 2011) between real and decoded
733 gaze path for model inference. The R^2 -score expresses the fraction-of-variance that our gaze decoding accounted for in the ground
734 truth gaze path.

$$R^2 = 1 - \frac{\sum_{i=1}^M (y_i - \alpha \hat{y}_i - \beta)^2}{\sum_{i=1}^M (y_i - \bar{y})^2} \quad (4)$$

735 with y_i the ground truth of sample i , \hat{y}_i the predicted value and \bar{y} the mean value. Unlike the Pearson correlation, or the squared
736 Pearson correlation, the R^2 -score used here is affected by the scaling of the data and can be arbitrarily negative.

737 **Decoding from the eyeballs and early visual cortex with time-shifted data**

738 To investigate if the decoding is instantaneous or further improves when temporal delays are being considered, we shifted the func-
739 tional image time series relative to the gaze labels. We again used the free-viewing dataset (Julian et al., 2018), because it featured the
740 most complex and natural viewing behaviors in our sample. For each image shift (0-10 TR's), we retrained the full model and tested it
741 on held-out participants using the across-participant decoding scheme.

742 To further assess whether DeepMRye can also be used to decode from brain activity directly, we used the same temporal shift-
743 ing procedure while decoding from area V1. The regions-of-interest mask was obtained by thresholding the Juelich-atlas mask "Vi-
744 sual_hOc1.nii" at 60 % probability and reslicing it to the resolution of our template space (Fig. S7). As the model is agnostic to the
745 dimensions of the input data, decoding from region-of-interests other than the eyeballs required no change in model architecture.

746 **Effect of training set size**

747 To evaluate how the number of participants in the training set influences decoding performance, we retrained the model using dif-
748 ferent subsets of participants across model iterations (1-21 participants). For each iteration, we tested the model on the same 6
749 participants, which were not part of the training set. To ensure that the results were robust and did not depend on individual details
750 of single participants used for model training, we repeated this procedure 5 times for each training-set size and then averaged the
751 results. To do so, we randomly assigned participants to the training set in each cross-validation loop while keeping the test set fixed.
752 Moreover, to avoid overfitting to these small training sets, we reduced the number of training epochs, using $e = 2 + N$ with N the
753 number of participants in the current training run and e the number of epochs. We kept the number of gradient steps in each epoch
754 constant ($n=1500$).

755 **Eyes-closed eye tracking**

756 As a proof-of-concept, we tested whether DeepMRye is capable of decoding gaze position, or rather the state of the eyeballs, while
757 the eyes are closed. We trained the model on the camera-based eye tracking labels of the 4 participants in dataset 6. We included
758 the data acquired with all 9 scanning protocols and with all viewing behaviors tested (fixation, smooth pursuit, and picture viewing).
759 We then evaluated the model on one participant, who was instructed to close the eyes and move them alternately from left to right
760 or up and down. The participant indicated the direction of movement by pressing a button which was used to color the coordinates
761 in (Fig. 3B). The participant performed this task nine times for one minute each. To reduce overfitting to the viewing behaviors in
762 the training set, we here used a higher dropout rate in the fully connected layers (drop ratio=0.5) than in our default model (drop
763 ratio=0.1).

764 Decoding at sub-imaging temporal resolution

765 Because different imaging slices are being acquired at different times, and because the MR-signal of a voxel could be affected by eye
766 motion within each TR, we tested whether our model is capable of decoding gaze position at sub-imaging temporal resolution. Across
767 different model iterations, we re-trained and re-tested the model using different numbers of gaze labels per TR ($n = 1-10$ labels), each
768 time testing how much variance the decoded gaze path explained of the true gaze path. Decoding different numbers of gaze labels
769 per TR was achieved by replicating the bottleneck layer n times, each one decoding gaze position for their respective time points using
770 a fully connected layer. Importantly, the weights between these layers were not shared, which allowed each layer to utilize a different
771 node in the bottleneck layer. Each layer could therefore capture unique information at its corresponding within-TR time point to
772 decode its respective gaze label. To keep the overall explainable variance in the test set gaze path constant, we always upsampled the
773 decoded gaze path to a resolution of 10 labels per TR using linear interpolation before computing the R^2 -score scores for each model
774 iteration. Potential differences in model performance across iterations can therefore not be explained by differences in explainable
775 variance. These final test R^2 -scores were range-normalized within each participant for visualization (Fig. 2F).

776 Functional imaging analyses

777 We tested whether the decoding output of DeepMRye is suitable for the analysis of functional imaging data by regressing it against
778 brain activity using a mass-univariate general linear model (GLM). This analysis was expected to uncover brain activity related to eye
779 movements in visual, motion, and oculomotor regions. To demonstrate that our approach is applicable even for natural and complex
780 viewing behavior, we conducted these analyses on the visual search dataset (Julian et al., 2018).

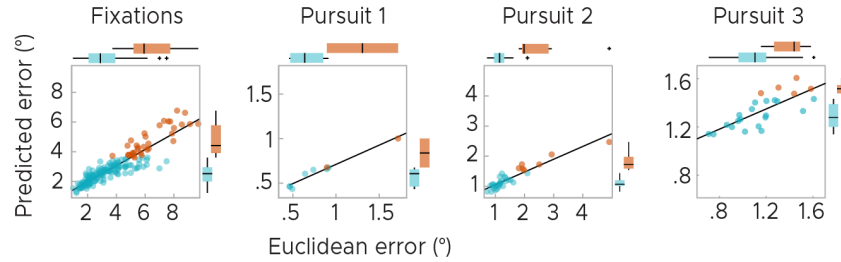
781 First, we decoded the median gaze position at each imaging volume using all cross-validation schemes described above. We then
782 obtained an approximate measure of eye movement amplitude by computing the vector between gaze positions of subsequent
783 volumes. Based on the vector length, or the amplitude of decoded putative eye movements, we built two regressors of interest; one
784 for far eye movements (>66 th percentile of movement amplitudes) and one for short eye movements (<33 rd percentile of amplitudes).
785 The mid-section was excluded to separate the modeled events in time. The two resulting regressors per scanning run were binarized
786 and convolved with the hemodynamic response function implemented in SPM12 using default settings. Head-motion parameters
787 obtained during preprocessing were added as nuisance regressors. Contrasting the resulting model weight between far and short
788 eye movements yielded one t-statistics map per participant.

789 To test which brain areas signaled the difference between far and short eye movements, we normalized the t-map of each participant
790 to MNI-space and smoothed it with an isotropic Gaussian kernel of 6mm (full-width-half-maximum). The smoothed statistical maps
791 were then used to compute an F-statistic on group level using SPM12. Moreover, to compare the results obtained with DeepMRye
792 to the ones of conventional eye tracking we repeated the imaging analysis described above using gaze positions obtained with a
793 conventional camera-based eye tracker. The final F-statistics maps were warped onto the fsaverage Freesurfer template surface for
794 visualization using Freesurfer (<https://surfer.nmr.mgh.harvard.edu/>).

795 **Supplementary Material**

Unsupervised predicted error correlates with true Euclidean error

A) Errors based on fixation target coordinates



B) Errors based on camera-based eye tracking

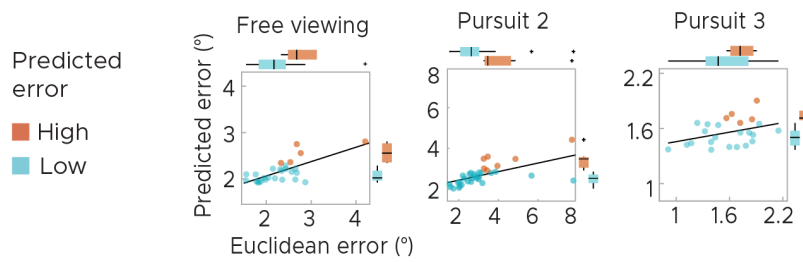


Figure S1: Predicted error (PE) correlates with the Euclidean error between real and predicted gaze positions. This allows to filter the test set post-decoding based on estimated reliability. A) Results plotted for models trained and tested using the fixation target coordinates. B) Results plotted for models trained and tested using labels acquired using camera-based eye tracking. We plot single-participant data with regression line. Participants were split into 80% most reliable (Low PE, blue) and 20% least reliable participants (high PE, orange). All scores expressed in visual degrees.

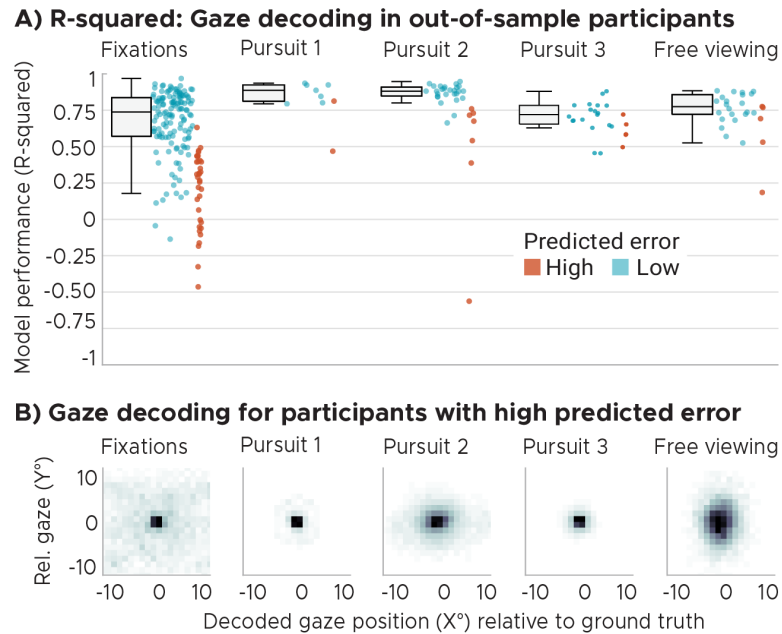


Figure S2: A) Gaze decoding group results expressed as the coefficient-of-determination (R^2). Top panel shows gaze decoding expressed as the R^2 -score implemented in scikit-learn (Pedregosa et al., 2011) between the true and decoded gaze trajectory for the five key datasets featuring fixations, 3x smooth pursuit and visual search. Note that R^2 can range from negative infinity to one. Participants are color coded according to predicted error (PE). We plot Whisker-box-plots for Low-PE participants and single-participant data for all. (B) Group-average spread of decoded positions around true positions collapsed over time in visual degrees for participants with high predicted error (orange dots in A).

Unsupervised detection of unreliable participants & samples

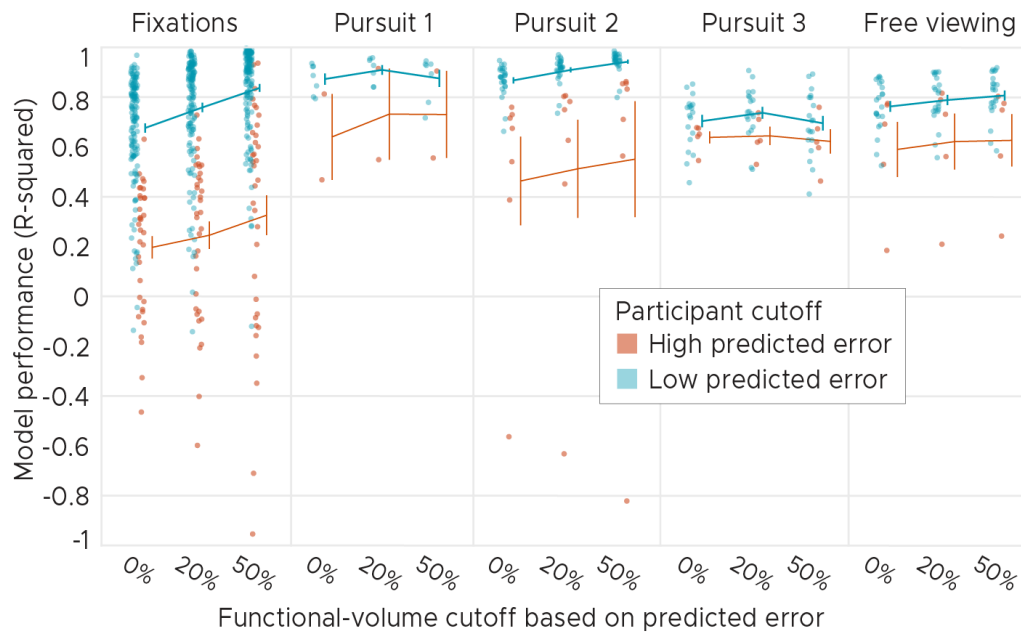
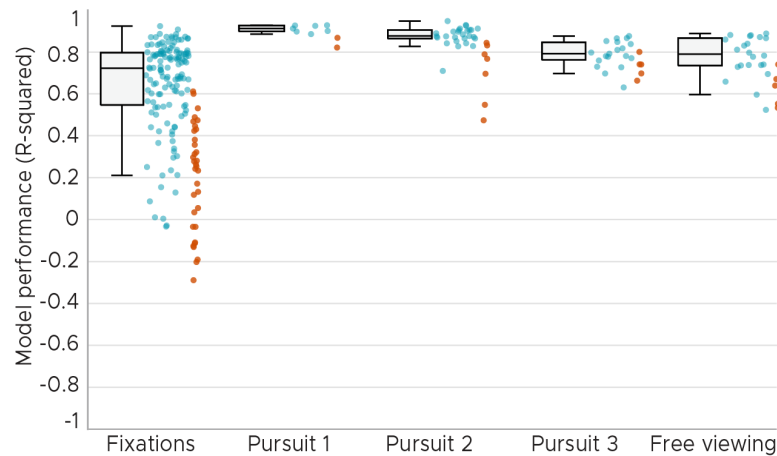


Figure S3: Model performance evaluated before and after exclusion of volumes with unreliable decoding. Here, before computing model performance we filtered out either the 0%, 20% or 50% least reliable volumes (i.e. those with the highest predicted error (PE)). Model performance is expressed as the coefficient-of-determination R^2 -score implemented in scikit-learn (Pedregosa et al., 2011) between true and decoded gaze trajectory for the five key datasets featuring fixations, 3x smooth pursuit and visual search. Note that R^2 can range from negative infinity to one. We plot single participant data (dots) as well as the mean \pm standard error of the mean. Participant dots were additionally color coded according to the participants' PE.

A) Gaze decoding across different within-participant partitions



B) Gaze decoding across datasets with similar scan protocols

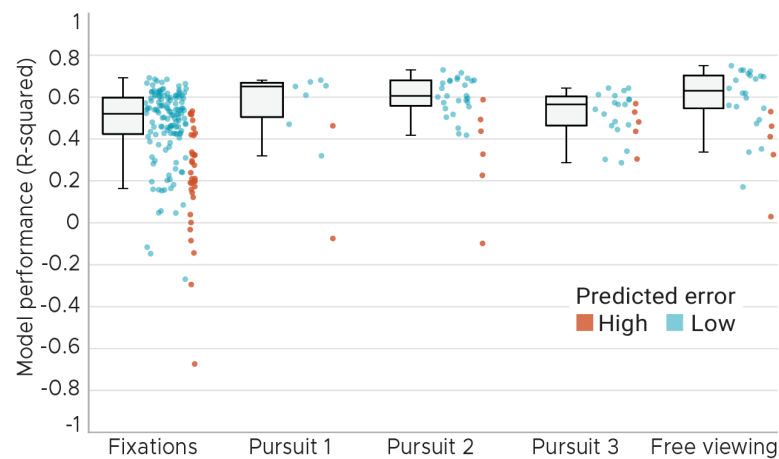


Figure S4: A) Within-participant gaze decoding obtained by training and testing the model on different data partitions of all participants within a dataset. B) Across-dataset gaze decoding obtained using leave-one-data-set-out cross-validation. We plot the R^2 -score as implemented in scikit-learn (Pedregosa et al., 2011) between true and decoded gaze trajectory for the five key datasets featuring fixations, 3x smooth pursuit and visual search. Note that R^2 can range from negative infinity to one. The results of datasets 1-3 were obtained using the fixation target labels, the ones of datasets 4-5 were obtained using camera-based eye tracking labels. Participants are color coded according to predicted error (PE). We plot Whisker-box-plots for Low-PE participants and single-participant data for all.

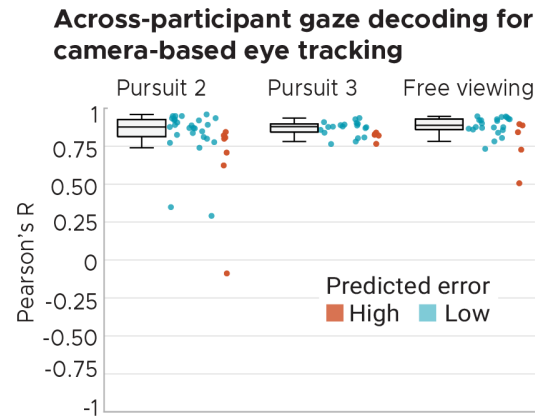


Figure S5: Gaze decoding evaluated using camera-based eye tracking for smooth pursuit datasets 3-4. Model performance expressed as the Pearson correlation between true and decoded gaze trajectory for the datasets with camera-based eye tracking. Because the visual search dataset 5 used labels obtained using camera-based eye tracking as well, we additionally plot the results obtained for this dataset again for the sake of completeness. Participants are color coded according to predicted error (PE). We plot Whisker-box-plots for Low-PE participants and single-participant data for all.

Effect of training set size for all viewing priors

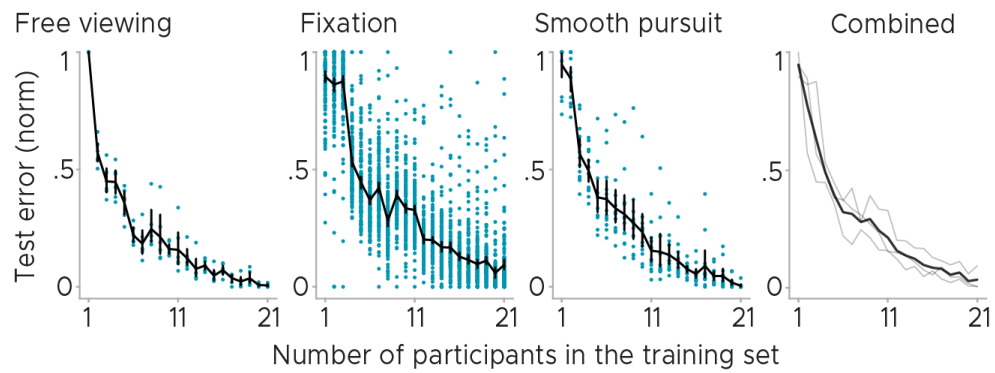


Figure S6: Normalized test error as a function of how many participants were used for model training plotted for three different viewing behaviors. We plot single participant data (dots) as well as the across-participant average model performance (black lines). Error bars depict the standard error of the mean. Right panel shows the average across datasets.

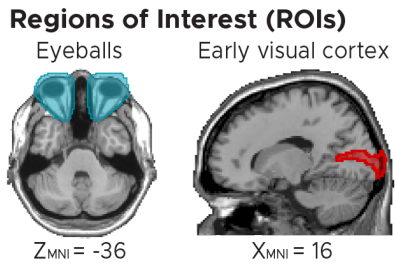


Figure S7: Visualisation of eyeball and visual cortex (V1) masks used for decoding in Figure 2E. Eyeballs were manually segmented in the structural scan of the SPM-template participant "Colin27". The V1 mask was obtained by thresholding the Juelich-atlas mask "Visual_hOc1.nii" at 60 percent probability. MNI coordinates added. For decoding, both masks were resliced to 2mm isotropic to match the voxel resolution of our template space.

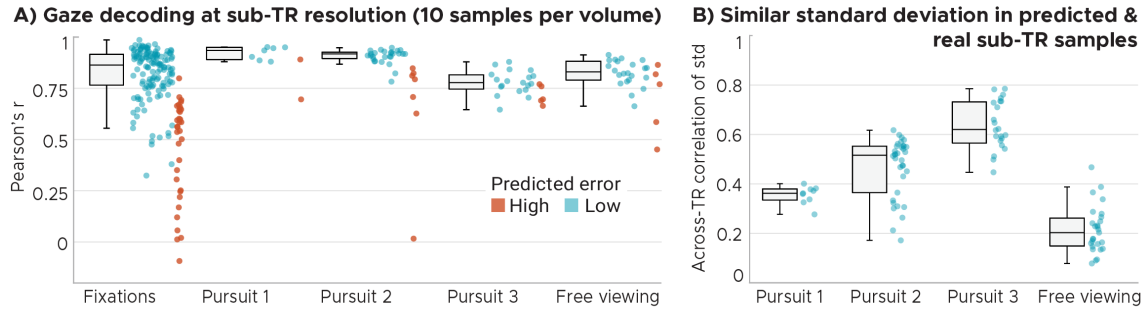


Figure S8: Sub-imaging decoding resolution. A) Group results when all 10 sub-TR samples are considered for computing the Pearson correlation between true and decoded gaze trajectories. Participants are color coded according to predicted error (PE). We plot Whisker-box-plots for Low-PE participants and single-participant data for all. **B)** Similar standard deviation of real and decoded gaze labels within each functional volume (TR), i.e. if the 10 real gaze labels of a TR had a high standard deviation (indicating larger eye movements within this TR) then the 10 decoded gaze labels showed a high standard deviation as well. We plot the Pearson correlation between the within-TR standard deviation computed using the full time course of each participant as Whisker-box-plots and single-participant data as dots.

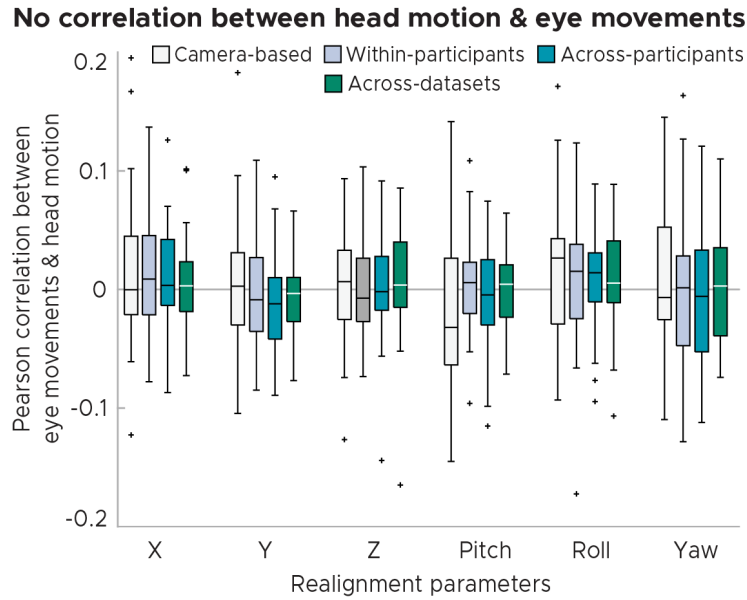


Figure S9: No correlation between eye movements and head motion in visual search dataset 5. Eye movements were computed as the vector length between gaze positions of subsequent volumes. Head motion estimates reflect the 6 SPM12-realignment parameters. We plot Whisker-box-plots of this correlation computed for gaze labels obtained with camera-based eye tracking as well as with three cross-validation schemes of DeepMReye (within-participant-, across-participant- and across-dataset prediction).

Instantaneous MR-signal fluctuations explained by eye movements (no HRF convolution)

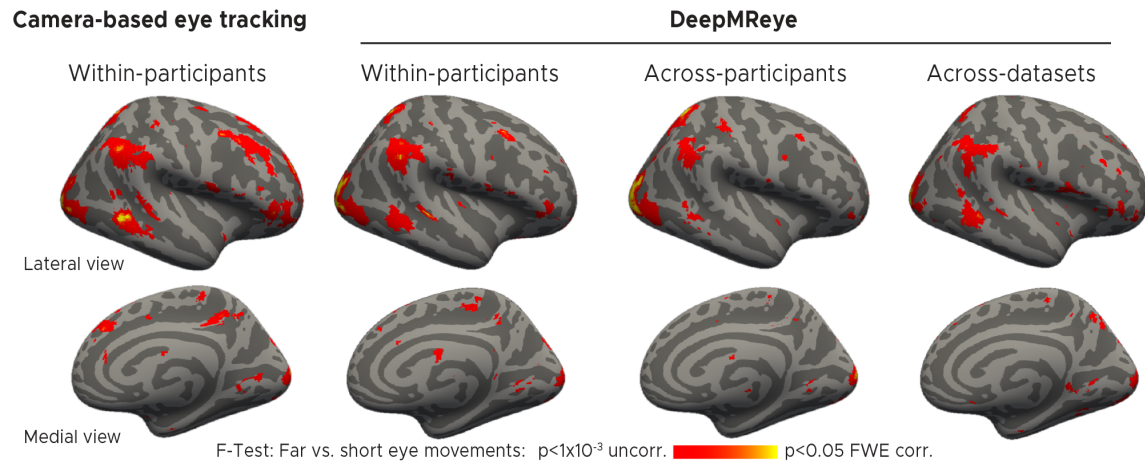


Figure S10: General-linear-model (GLM) group results for the contrast 'Far vs. short eye movements' during visual search without accounting for the hemodynamic response function. We plot the F-statistic of this contrast superimposed on a template surface (fsaverage) for gaze-labels obtained with camera-based eye tracking (first panel) as well as for three DeepMReye cross-validation schemes. Within-participants: All participants of a dataset were included with different partitions in model training and test. Across-participants: Different participants were included during model training and test. Across-datasets: Different datasets (and hence also different participants) were included during model training and test.